DENSITY FUNCTIONAL THEORY STUDY OF TiO_2 BROOKITE (100), (110) AND (210) SURFACES DOPED WITH RUTHENIUM (Ru) AND PLATINUM (Pt) FOR APPLICATION IN DYE SENSITIZED SOLAR CELL

BY

DIMA RATSHILUMELA STEVE

(15017654)

THESIS

PRESENTED IN FULFILMENT FOR THE REQUIREMENTS OF MASTERS OF SCIENCE (M.Sc.) DEGREE

IN

PHYSICS

SCHOOL OF MATHEMATICS AND NATURAL SCIENCES

AT THE

UNIVERSITY OF VENDA

SUPERVISOR: Dr E.N MALUTA (UNIVEN)

Co- SUPERVISOR: Prof R.R MAPHANGA (CSIR)

YEAR: 2017

DECLARATIONS

I, Ratshilumela Steve Dima declare that this research report submitted to University of Venda for the degree of MSc in Physics has not been previously submitted for a degree at any other university. The references that helped me compile this document are fully cited.

Signed by _____ at_____ on the _____ day of _____ 2017

DEDICATIONS

I would like to dedicate this dissertation to my family: my Dad, Mom and my two sisters for their moral support throughout my studies. Above all I would love to dedicate this to almighty God for daily support and protection.

ACKNOWLEDGEMENT

I would love to extend my gratitude to my supervisor Dr E.N Maluta and my Co-supervisor Prof R.R Maphanga for helping me out throughout this research. I also like to thank my friends Muravha A.E, Dzivhani M, Mahlangu N, Mphephu N and Khedzi TT for their friendship and support throughout my MSc degree. Not forgetting my lab co-workers for their assistance. I would also want to extend my gratitude to the department of physics for the opportunity to proceed with my studies in honours. Lastly, I would like to kindly acknowledge the National Institute for Theoretical Physics (NITheP) for financial support.

ABSTRACT

Since the discovery of water photolysis on a TiO_2 electrode by Fujishima and Honda in 1972, TiO_2 has attracted extensive attention as an ideal photocatalytic material because of its excellent properties such as high activity, good stability, nontoxicity and low cost. Hence, it has been widely used in the fields of renewable energy and ecological environmental protection. However, as a wide band gap oxide semiconductor ($E_g = 3.14$ eV), brookite TiO_2 can only show photocatalytic activity under UV light irradiation ($\lambda < 387.5$ nm) that accounts for only a small portion of solar energy (approximately 5 %), in contrast to visible light for a major part of solar energy (approximately 45 %). Therefore, effectively utilizing sunlight is the most challenging subject for the extensive application of TiO_2 as a photocatalyst. Due to the unique d electronic configuration and spectral characteristics of transition metals, transition metal doping is one of the most effective approaches to extend the absorption edge of TiO_2 to the visible light region. This method of doping either inserts a new band into the original band gap or modifies either the conduction band or valence band, improving the photocatalytic activity of TiO_2 to some degree. In this work, the structural, electronic and optical properties of doped and undoped TiO_2 (100), (110) and (210) surfaces were performed using first principle calculations based on DFT using a plane-wave pseudopotential method. The generalized gradient approximation was used in the scheme of Perdew-Burke-Ernzerhof to describe the exchange-correlation functional as implemented in the Cambridge Sequential Total Energy Package code in the Materials Studio of BIOVIA. The metal dopants shift the absorption to longer wavelengths and improves optical absorbance in visible and near-IR region. The un-doped (210) surface showed some activity in the visible and near IR region.

Table of Contents

LIST OF FIGURES

LIST OF TABLES

LIST OF ABBREVIATIONS

CASTEP	-	Cambridge Sequential Total Energy Package
CB	-	Conduction Band
CBE	-	Conduction Band Energy
CdTe	-	Cadmium Telluride
CuInGaSe	-	Copper Indium Gallium Selenide
DSSC	-	Dye-Sensitized Solar Cell
DFT	-	Density Functional Theory
DOS	-	Density of States
E_{FB}	-	Flat Band Potential
E_f	-	Fermi Level
E_g	-	Energy Gap
GGA	-	Generalized Gradient Approximation
LDA	-	Local Density Approximation
PWGGA	-	Perdew-Wang Generalized Gradient Approximation
Pt	-	Platinum
PV	-	Photovoltaics
Ru	-	Ruthenium
SCF	-	Self-Consistent Field
TiO_2	-	Titanium Dioxide

UV	-	Ultraviolet
VB	-	Valence Band
VBE	-	Valence Band Energy

CHAPTER 1

1.1 General Introduction

The world energy consumption is increasing rapidly from year to year. In 1998, it was reported to be 12.7 TW, and is expected to be approximately between 26.4 to 32.9 TW in 2050. This is predicted to increase to between 46.3 to 58.7 TW by 2100 [1]. The yearly increase in the world energy consumption will result in the increase of demands towards natural resources such as coal, petroleum, and natural gas. Thus, the world is facing an energy crisis, which has a great impact on the development of the economies worldwide [1]. Consequently the need for alternative and renewable sources of energy, which are environmentally friendly is imperative.

South Africa is a developing country and its economy is derived mainly from manufacturing and mining, which are mostly energy-intensive industries. Despite the fact that it has some of the cheapest electricity supplies, South Africa's use of energy has not been particularly efficient [2]. South Africa has only one provider of electricity, a state entity called Eskom. Recently, Eskom has admitted that electricity supply will be highly constrained for at least the next five years, due to the drastic deterioration of power stations and the depletion of coal [2].

Solar energy is the most available renewable energy on earth, which is becoming more widely used to generate electrical power all around the world due to its environmental, economic and strategic benefits [3]. Photovoltaics (PV) and the solar thermal generators are the two main technologies which are used to convert solar energy into electricity [3]. Apart from these, other technologies such as wind power and biogas have recently been considered to supply energy in some countries [3, 4].

This research is focused on using computer simulation methods to simulate components for PV systems, i.e., materials for dye-sensitized solar cells (DSSCs), which were invented in 1991 by M. Grätzel [5]. DSSC are the most promising inexpensive way towards harvesting sunlight, which can be converted to useable electricity. Despite the fact that extensive work has been done in DSSC's research, there are still some factors within the field that are overlooked, for instance bonding and reaction mechanisms between the dye molecules and TiO_2 surface. Therefore the current work focuses on the theoretical study of the brookite TiO_2 band gap

engineering by doping of the TiO_2 surfaces with different elements. Simulations are performed using computational modelling methods, in particular, density functional theory to investigate the effect of doping (with ruthenium and platinum elements) on various surfaces of brookite TiO_2. The low index TiO_2 surfaces of brookite are investigated, whereby structural, electronic and optical properties are calculated.

1.1.1 Solar Cells

Capturing of solar radiation and converting it to electricity or chemical fuels remain a huge challenge. Photovoltaic devices are the primary solar radiation conversion systems to harvest the solar radiation as a source of energy. These devices are more simply known as solar cells, they convert the incident photon energy of the solar radiation into electrical energy through the generation and subsequent collection of electron-hole pairs. There are several challenges that need to be looked at in research and development of solar cell technologies to make it a pragmatic solution to the energy crisis. The challenges include [4]:

- increasing power conversion efficiency
- reducing the cost
- increasing the stability
- using abundant and biocompatible raw materials.

1.1.2 Photovoltaic Generations

Photovoltaics are categorized into four generations based on their performance and cost effectiveness. The first generation of solar cells has a relatively higher efficiency with expensive production cost [5]. They are the classical example of solar cells. Photogenerated electron-hole pair is separated and collected through the p-n junction of a doped semiconductor, mainly silicon. The commercial market is dominated by this generation, due to their high efficiency however compered with high cost.

The second generation of solar cells is the thin film solar cells based on CdTe or CuInGaSe. These solar cells have a lower efficiency, but are much cheaper to produce and employ a less extensive fabrication process. Using the thin film technology, the cell thickness has been reduced from about a millimetre thick down to just a few microns, making possible a production cost of $0.73 per Watt in 2011 [6]. The

drawback for the 1st and 2nd generations is that they are limited by the Shockley-Queisser theoretical limit of ~30 % for a single p-n junction [7].

Third generation solar cells are very different from the first two generations because innovative semiconductors were used in here. Types of solar cells introduced in this generation includes (i) nanocrystal solar cells, (ii) photoelectrochemical cells, (iii) dye-sensitized solar cells, (iv) dye sensitized hybrid solar cells, (v) polymer solar cells. Nanocrystal solar cells are based on silicon substrate with coating of nano crystals. A thin film of nano crystals is used along with an Si substrate, which is obtained by a process called spin coating. Photoelectrochemical cells (PEC) consists of a semiconducting photoanode, which work best with electrons and can also separate salacity of semiconductors. DSSCs (Gräetzel cells) use photoelectrons to increase power efficiently. Dyes are made of metal organic complex and the molecules are hit by increasing heat. Polymer solar cells were the last invention of this generation and are characterised as being lightweight, inexpensive, flexible and disposable on any molecular level. Thus, they have little impact on environment.

Fourth generation of solar cells, are the most successful types of solar cells for mankind and those are hybrid nanocrystal cells. For this generation polymers and nano particles are mixed to make a layer from which electrons and protons are able to move produce better voltage and good quality direct current.

1.1.3 Classical p-n Junction Solar Cells

The 1st and 2nd generation photovoltaic devices consist of a p-doped and an n-doped semiconductor placed in contact to form a junction. A schematic representation of a p-n junction solar cell is shown in Figure 1.1. Without the presence of an external applied bias, an electric field is formed at the junction (depletion region) due to the inter-diffusion of majority charges [7]. Photon absorption from sunlight at the depletion region generates electron-hole pair which gets separated by the built-in electric field. As long as the separated charges come out of the depletion region, they become the majority carrier and can be collected at the positive and negative contacts giving rise to the cell current [7, 8].

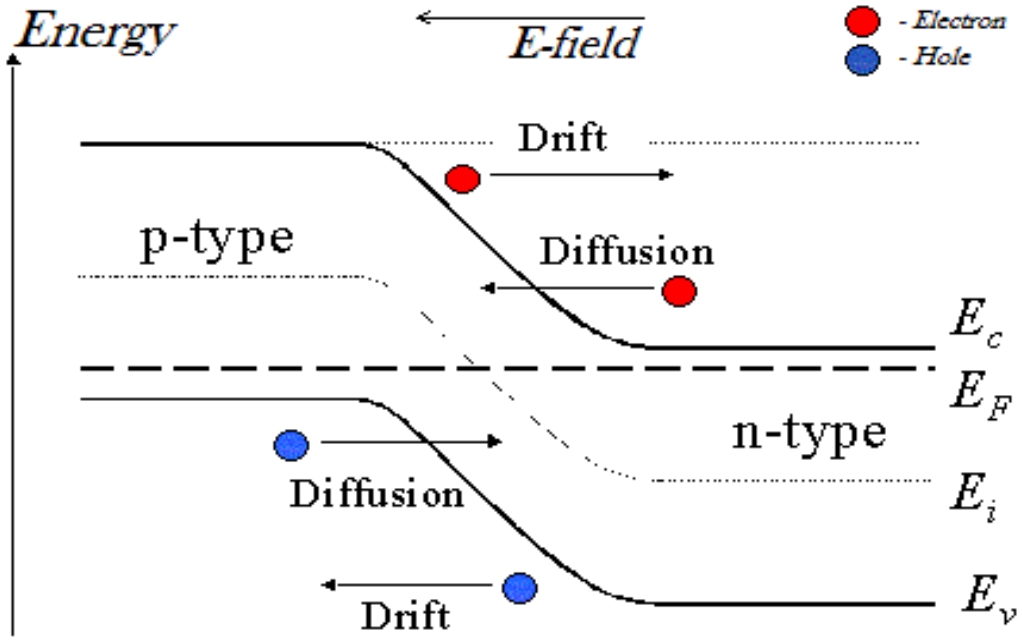

Figure 1. 1 Schematic representation of charge separation in a p-n junction [7]

1.2 TiO_2 Polymorphs

1.2.1 Background

TiO_2 is a versatile material, which is widely used in our daily lives due to its numerous strengths, such as brightness, stability, and high refractive index. The traditional applications of TiO_2 include paint and coating (enamels), plastics, paper, inks, fibbers, food, pharmaceuticals, toothpaste, and cosmetics. Recently, TiO_2 has received considerable attention for its promising applications in the environment, energy, information fields; such as photocatalysis, photovoltaics and batteries and data storage respectively [9, 10]. For these applications, especially photocatalysis and photovoltaics, widely used TiO_2 particles have limitations, such as large band gap (3.2 eV) and slow carrier transport. Large band gap implies inefficiency in utilization of solar light, which slow carrier transport increases the chance of recombination. Effects of doping, morphology control, and surface treatment are being investigated. Recent studies have shown that modified TiO_2 structures could be used more efficiently in applications such as photocatalysis, solar cells (especially in dye sensitized solar cells) [11].

1.2.2 TiO_2 Properties

There are three common polymorphs of TiO_2 namely; (i) rutile phase with a tetragonal, space group of $P4_2/mnm$ and E_g ~ 3.05 eV, (ii) anatase phase with a tetragonal space group of I41/amd and E_g ~ 3.23 eV and (iii) brookite phase with orthorhombic, Pbca, E_g ~ 3.26 eV) [4, 6]. Crystal parameters are a = 4.594 Å, c = 2.959 Å for rutile, a = 3.785 Å, c = 9.514 Å for anatase and a = 5.456 Å, b = 9.182 Å, c = 5.143 Å for brookite. Their representative unit cells are illustrated in Figure 1.2. Rutile is the most thermodynamically stable phase with an energy of approximately 1.2-2.8 kcal/mol more than the other phases [4]. Anatase is a metastable phase, and it shows superior photocatalysis performance because of fast carrier transport and less recombination. The metastable anatase transforms to rutile phase irreversibly at the temperature between 700 °C and 1000 °C, which is determined by several factors including crystallite size and impurity levels.

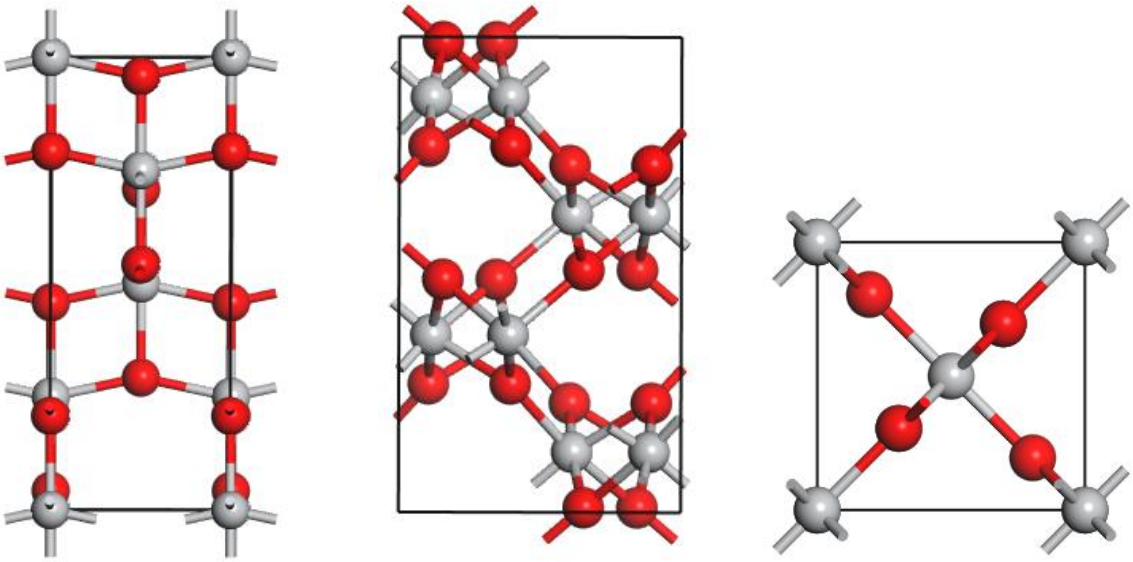

Figure 1. 2 The schematic representation of conventional cells for (a) anatase, (b) brookite and (c) rutile TiO_2 systems. The grey spheres represent Ti atoms while red spheres represent O atoms.

The crystal structures of TiO_2 polymorphs are described as an octahedron frame of oxygen, composed of one titanium cation located at the center and six oxygen anions occupying the corners. Each oxygen corner is shared by three octahedral resulting in

1:2 (Ti:O) stoichiometric configuration [11]. There are multiple methods with satisfying stoichiometric requirement since sharing could be corner, edge, and/or face. Each octahedron in the rutile TiO_2 is surrounded by ten neighbouring octahedra (two sharing the edge of the octahedron and eight sharing the corner of the octahedron. In the anatase structure, each octarhedron is in contact with eight octahedra (four sharing the edge and four sharing the corner). The brookite structure is composed of octahedra, each with a titanium atom at its center and oxygen atoms at its corners. The octahedra share edges and corners with each other to such an extent as to give the crystal the correct chemical composition. The octahedra are distorted and present the oxygen atoms in two different positions [4]. The bond lengths between the titanium and oxygen atoms are different. Octahedra arrangement produces a crystalline structure with tunnels along the c-axis, in which small cations such as hydrogen or lithium can be incorporated.

1.3 Applications of TiO_2

The most important application areas for TiO_2 are in paints and varnishes as well as paper and plastics, which account for approximately 80 % of the world's titanium dioxide consumption. Other pigment applications such as printing inks, fibers, rubber, cosmetic products and foodstuffs account for the other 8 % [5]. The rest is used in other applications, for instance the production of technical pure titanium, glass and glass ceramics, electrical ceramics, catalysts, electric conductors and chemical intermediates. It is also used in most red-coloured candy.

Photocatalytic behaviour of TiO_2 has been extensively explored since it was discovered in the 1970s [5]. When TiO_2 is exposed to Ultra-Violet (UV) light, the light is absorbed and electron/hole pairs are generated in the conduction and valence bands. Holes in the valence band will oxide/mineralize pollutant target directly or indirectly (via mediator hydroxyl radical). If the adsorbed molecule is O_2, it will react with an electron from the conduction band to generate a hydroxyl radical as described in the second set of reactions [9].

The photocatalytic reaction is schematically explained in Figure 1.3. Since this redox reaction based mineralization has power to decompose toxic pollutants such as 4-chlorophenol, benzene, it has been widely used in water treatment and surface self-

cleaning. Due to its nature using solar light, the photocatalysis based system can be installed both in rural and urban areas without an external power source [10]. For example, noxer block is a cement mortar block with a TiO_2 surface layer which treats pollutants in the air. This converts nitrogen oxides (NO_x) to harmless nitrate ions by using the sunlight. Tens of towns in Japan and England have placed the noxer blocks in street paving [10].

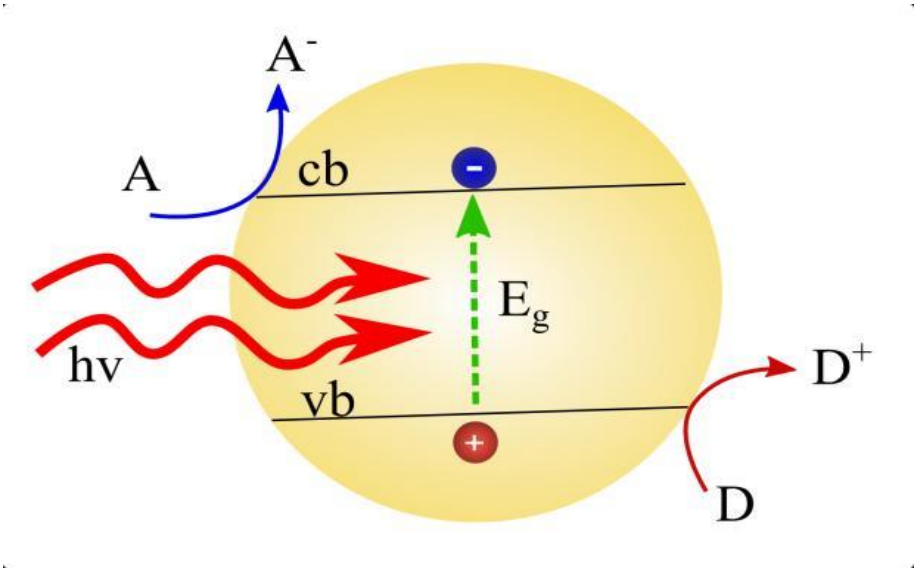

Figure 1. 3 Simplified diagram of heterogeneous photocatalytic process [10].

Another application of photocatalysis is water splitting and CO_2 reduction, both of which utilize the electrons that are optically excited to the conduction band [10, 11]. Photocatalytic splitting of water by TiO_2 has received a considerable amount of attention. For hydrogen production, the conduction band and valence band edges should be well matched with the redox potentials of water, as shown in Figure 1.4. The conduction level should be higher than hydrogen production level (EH_2/H_2O) while the valence band should be lower than water oxidation level (EO_2/H_2O). Electrons and holes will be generated on the semiconductor site, and holes generate O_2 at semiconductor site, while electrons will migrate to counter electrode to execute reduction forming H_2. In addition to that, materials should be chemically stable to resist photo-corrosion and have long lifetime of electron/hole pairs [8]. TiO_2 is a suitable material from the viewpoint of band arrangement and chemical stability requirement.

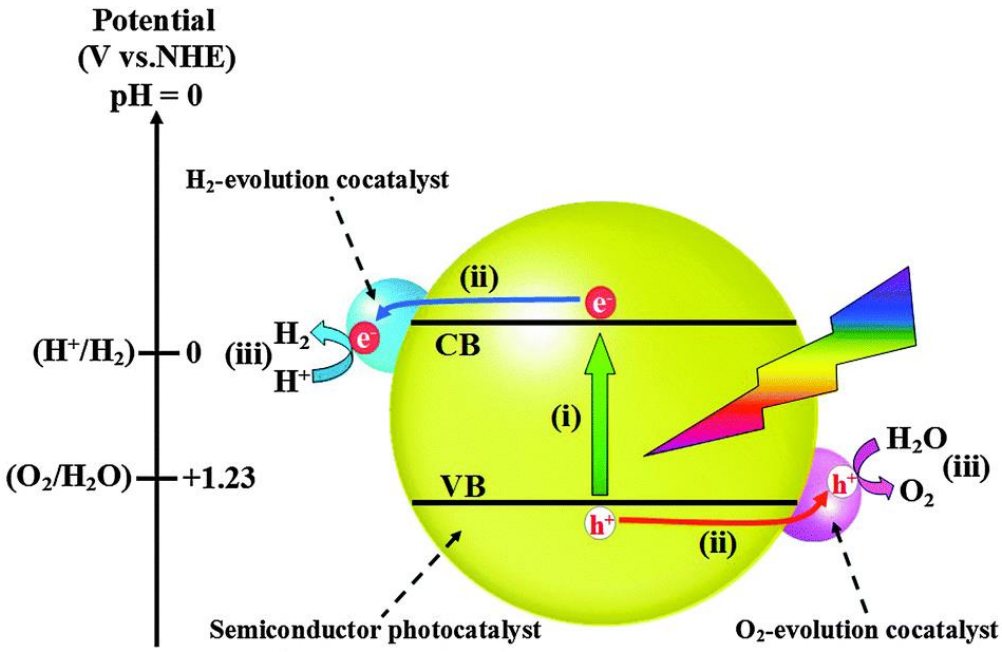

Figure 1. 4 Mechanism of TiO_2 photocatalystic water splitting for hydrogen production [12].

One kind of photoelectrochemical cells that is applied to water splitting is schematically illustrated in the left plot of Figure 1.4. An interesting development is the deployment of particulate and colloidal semiconductor [9-12]. Particulate semiconductor consists of a wide band gap semiconductor (such as TiO_2) powder or colloid and a noble metal (such as Pt) which is fused to semiconductor to work as co-catalyst. The system is a miniature of photoelectrochemical cell, and mixed H_2 and O_2 are formed at same place. The roles of co-catalyst are to lower the electrochemical over-potentials associated with the multi-electron water oxidation and reduction reaction and provide an interface to enhance electron-hole separation. RuO_2 and IrO_2 are best known catalysts for water oxidation, whereas noble metals (Pt, Pd, and Ni) are commonly used as water reduction elements. In this particulate paradigm, photocatalysis can take place in the homogeneous phase without the requirement of expensive transparent electrodes and without the need for directional illumination.

Dye-sensitized solar cells (DSSCs) are considered to be promising candidates for low-cost harvest of solar energy using sustainable and environmentally friendly materials [4]. In general, DSSCs consist of three parts: the dye-sensitized TiO_2 nanocrystalline porous film photoanode on a transparent conducting glass, an electrolyte solution penetrating throughout the TiO_2 anode film, and the platinized

transparent conducting oxide (TCO) glass as the counter electrode [5,6]. Among the abovementioned three parts, the TiO_2 nanoparticles based photoanode is considered to be the main limiting factor against achieving the theoretically predicted high efficiency (31 %) because of the presence of large number of grain boundaries (more electron recombination losses) and poor utilization of near infrared light [7]. Hence the importance of understanding reaction mechanisms between molecules and TiO_2 surfaces.

1.3.1 Dye Sensitized Solar Cells

A dye-sensitized solar cell is another class of photoelectrochemical cells, which converts solar light to electric energy by using inorganic semiconductors and sensitizers [13]. DSSCs offer moderate conversion efficiency with other advantages, such as low production cost, easy scale-up, good performance under weak/diffuse light, and compatibility with building window glass and flexible substrates. Therefore, DSSCs are regarded as one of promising alternatives to bulk silicon-based solar cells, which is currently dominant in the market.

The history of the dye sensitizer is very long. However, the energy conversion efficiency of the devices stayed as low as 1 % until Grätzel *et al*. carried out a milestone research and invented a current structure of DSSCs in early 1990s [13-15]. The breakthrough made in Grätzel's cell is the introduction of TiO_2 nanoparticle based photoanode with extremely high surface area [16]. A thin layer of dye is coated on the surface of TiO_2 porous film that preferentially collects the photogenerated electrons from the dyes. The energy conversion efficiency of the first Grätzel's cell was 7.1 % [5].

For the last two decades, DSSCs have been extensively studied, which covers the areas of fundamental physics, device operating mechanism, material innovation, and novel structure design [13]. This leads to the significant increase on the performance of the solar cells and the reduced manufacturing cost [12, 17-19]. Currently, the efficiency of DSSCs manufactured by Sharp reaches upto 10.4 % and the efficiency of the submodule produced by Sony goes up to 9.2 % [20]. In the lab scale, the best efficiency of DSSCs has already surpassed 11 % [20-22].

Major differences of DSSCs from other semiconductor solar cells are that the solar light is not mainly absorbed by the semiconductor (TiO_2) and that the electron-hole pair is not separated by the built-in-potential of a p-n junction [8]. A visible component of the solar light generates electron-hole pairs in the dye sensitizer which is anchored on the photoanode of wide bandgap semiconductor nanoparticles. When the electron-hole pairs are formed in the dye molecules, they are quickly separated at a picosecond scale due to the difference in energy levels. Electrons are injected from the dye to the conduction band of the photoanode, and are transferred to the transparent conducting oxide (TCO) film that is coated on the glass. Holes in the dye molecules are delivered to the electrolyte through a redox reaction [22]. In these types of solar cells, the maximum output voltage is the difference between Fermi energy of the semiconductor film and redox potential of the electrolyte. The operating principle of DSSCs and the potential source for a back-electron transfer is schematically summarized in Figure 1.5.

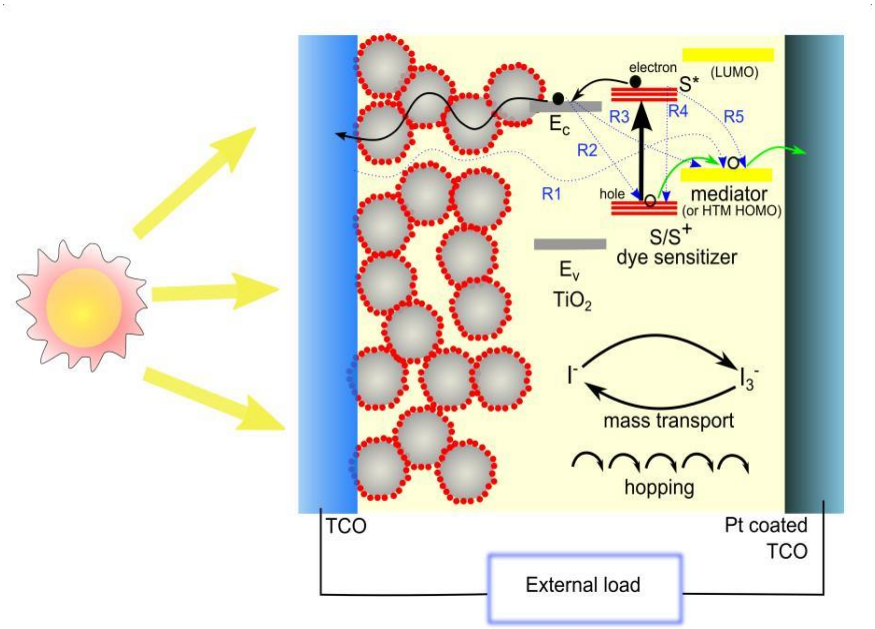

Figure 1. 5 Schematic representation of dye-sensitized solar cell [23].

The photoanode acts as electron transport path, light path, and dye anchoring scaffold. It is one of the most important components in DSSCs. Carrier injection, transport, trapping, and recombination are closely related to material, morphology and phase of photoanode. A dye sensitizer is a major component to absorb incoming solar light generating electron/hole pairs. The role of a sensitizer requires its well matched

energy level to facilitate efficient electron injection and dye regeneration, strong physical anchoring to the photoanode, sufficient absorption of solar light, and stable operation for a long period. Metal-complex, metal-free organic dye, natural dye, and quantum dot have been used as sensitizing materials [23]. Electrolytes perform a mediator function to deliver hole through redox reaction or direct hole transport. It can be divided into organic solvent liquid, solvent free liquid, quasi-solid, and solid electrolytes. The highest efficiency DSSCs are made of organic solvent liquid electrolyte due to its fast ion diffusion and ease of infiltration [24]. The commonly employed redox couple is I-/I3- pairs. Transparent conducting oxide plays a pivotal role in optoelectrical devices, fulfilling the function of light transmittance and conducting electrode simultaneously. In DSSCs, TCO is additionally required to be chemically stable, endure corrosive electrolyte and high temperatures due to the partial sintering process of TiO_2 photoanode [23-25].

1.4 Purpose of the Study

1.4.1 Aim

The aim of the study was to use first principle density functional theory to investigate the adsorption of ruthenium and platinum on brookite TiO_2 surfaces for application in dye-sensitized solar cells.

1.4.2 Objectives

The objectives of the study were to:

- determine the convergence parameters (energy cut-off and k-points) for bulk TiO_2 brookite polymorphs
- optimize the bulk structure of TiO_2 brookite polymorph
- cleave (1 0 0), (210) and (110) surfaces from TiO_2 bulk structure
- optimize the cleaved surfaces and calculate their electronic properties
- dope TiO_2 optimized surfaces with ruthenium and platinum separately
- calculate structural and electronic properties of Ru and Pt-doped TiO_2 surfaces.

CHAPTER 2

2.1 Literature Review

2.1.1 Brookite TiO_2 Structure

Brookite is the orthorhombic variant of titanium dioxide, which occurs in four natural polymorphic forms (minerals with the same composition but different structure). The International Mineralogical Association (IMA) recognizes these four forms; the others are akaogiite (monoclinic), anatase (tetragonal) and rutile (tetragonal). Brookite is rare compared to anatase and rutile and, like these forms, it exhibits photocatalytic activity [4]. It has a larger cell volume than either anatase or rutile, with 8 TiO_2 groups per unit cell, compared with 4 for anatase and 2 for rutile [6]. Iron Fe, tantalum Ta and niobium Nb are common impurities found in brookite TiO_2 [4].

Figure 2. 1 Crystal structure of TiO_2 brookite from Baluchistan [4].

The brookite structure is built up of distorted octahedra with a titanium ion at the center and oxygen ions at each of the six vertices. Each octahedron shares three edges with adjoining octahedra, forming an orthorhombic structure.

Crystals are typically tabular, elongated and striated parallel to their length. They may also be pyramidal, pseudo-hexagonal or prismatic. Brookite and rutile may grow together in an epitaxial relationship [4]. Brookite is usually brown in colour, or sometimes yellowish or reddish brown, or even black. Beautiful, deep red crystals (seen in Figure 2.1) similar to pyrope and almandite garnet are also known. Brookite displays a submetallic luster. It is opaque to translucent, transparent in thin fragments and yellowish brown to dark brown in transmitted light [6].

2.1.2 Preparation of Brookite

Brookite is not just the rarest of the four natural TiO_2 polymorphs, it is also the most difficult phase to prepare in the laboratory. The first synthesis of brookite dates back to the late 1950s. Classically, brookite was synthesized from titanium (IV) compounds in aqueous or organic media by hydrothermal methods at high temperatures and pressures. Mixtures of anatase and brookite were prepared by thermal treatment of the amorphous TiO_2 powders obtained by hydrolysis of titanium (IV) tetraethoxide [26-27]. With the aim of synthesizing a pure brookite, Yamaguchi found that a film of brookite was obtained on the surface of a Ti foil by anodization in a solution of H_2SO_4 (50 % by weight) [28].

Kominami *et al*. [29] produced microcrystalline brookite titania of ~ 50 nm size by thermal treatment of oxobis (2, 4-pentanedionato-O, O′) titanium in ethylene glycol in the presence of sodium laurate and a small amount of water in an autoclave at 300 °C. The study showed that sodium salts, water and the organic titanium complex as the titanium source were indispensable for the formation of brookite crystals. Ethylene glycol as the reaction medium was essential to minimize the formation of other phases of titania. This brookite TiO_2 began to directly transform to rutile phase on calcination at around 700 °C and completely converted at 900 °C. Lee and Yang [30] reported on synthesis of mixture of brookite and rutile titania by hydrolysis of $TiCl_4$ in HCl. The proportion of the two phases was dependant on the acidity and the aging time. Their findings showed that the maximum of 80 % yield of brookite phase with 20 % being anatase.

Pure brookite was first synthesized by Keesmann in 1966 [31], using hydrothermal treatment of amorphous TiO_2 obtained by hydrolysis of titanium tetraisopropoxide or

alkaline titanates, in the presence of a solution of NaOH containing 3–25 atomic % of Na with respect to (Ti^+ Na). Na^+ ions were considered to stabilize the lattice of brookite. Later, Schwarzmann and Ognibeni [31] obtained well crystallized brookite by hydrothermal treatment of $TiO_2 \cdot xH_2O$ between 100 °C and 300 °C in the absence of Na^+ ions.

As solution-processable and low-cost semiconductors, organ lead halide perovskites are attracting enormous attention for application as promising photovoltaic absorbers capable of high-power conversion efficiency over 20 %. Kogo *et al*. [32] reported a mesoporous layer of titanium oxide, which requires sintering at high temperature (400–500 °C) and serves as an efficient electron collector as well as a scaffold for crystal nucleation. To enable the rapid low-cost manufacture and construction of lightweight flexible solar cells built on plastic films, a sinter-free electron collection layer (mesoporous and compact layer) is required. Kogo *et al*. [32] synthesized a highly crystalline layer of brookite (orthorhombic TiO_2), which was prepared by a sinter-free solution process as an efficient mesoporous electron collector. Strong inter-particle necking of the brookite nanoparticles by a dehydration–condensation reaction enabled the formation of a highly uniform mesoporous layer at low temperature (130–150 °C). In comparison with an anatase TiO_2 mesostructure prepared by high temperature (500 °C) sintering, the brookite electron collector exhibits a photovoltaic performance with a greater fill factor and 100 mV-higher open-circuit voltages is shown in Figure 2.2 below [32].

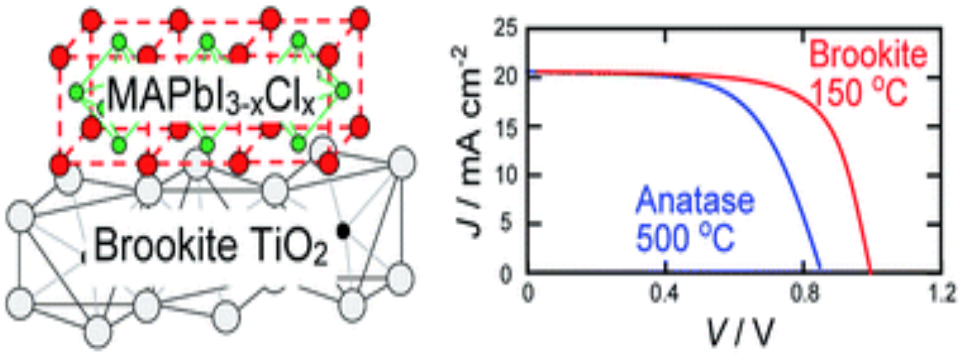

Figure 2. 2 Illustrates the doping of brookite (left) and its comparison of the photovoltaic performance to that anatase (right).

2.1.3 Electronic Structure of Brookite

The knowledge of the electronic band structure of the TiO_2 polymorphs is useful to understand the photocatalytic behaviour of the pure phases and of their mixtures. The highest and lowest energy levels of a band are referred to as the band edges. As with molecular orbitals, the energy bands of interest are the highest occupied (called the valence band) and the lowest unoccupied (called the conduction). It is the energy gap (the band gap) between these bands (i.e., the difference in energy between the upper edge of the valence band and the lower edge of the conduction band) that determines the properties of the semiconductor. Theoretical and experimental work reported band gap values for brookite to be either smaller or larger than that of anatase [33].

In 1985, Grätzel and Rotzinger [33] were the first to estimate the band gap value, E_g for brookite TiO_2 as 3.14 eV by extended Hückel molecular orbital calculations. The E_g was intermediate between those of anatase (3.23 eV) and rutile (3.02 eV). Mo and Ching [33] studied the electronic structure and the optical properties of anatase, brookite and rutile using the self-consistent orthogonalized linear combination of atomic orbitals method. According to their calculations, brookite had a direct band gap of 2.20 eV, which is larger than that of anatase and rutile (1.78 eV for rutile and 2.04 eV for anatase, respectively). These results, as reported by the same authors, were an underestimation of the effective band gap values [33].

Zallen and Moret [34] reported the optical absorption edge of brookite TiO_2 which was measured at room temperature, using natural crystals. The measurements extend up to 3.54 eV in photon energy and 2000 cm^{-1} in absorption coefficient. The observed absorption edge is broad and extends throughout the visible spectrum, quite different from the steep edges of rutile and anatase. No evidence of a direct gap is seen in the range measured. The spectral dependence of the absorption strongly suggests that the brookite form of TiO_2 is an indirect-gap semiconductor with a bandgap of about 1.9 eV [34].

The flat band potential, (E_{FB}), of a semiconductor is a fundamental property for the thermodynamics of the interfacial electron transfer steps. For an n-type semiconductor such as TiO_2, it can be assumed that the positions of the flat band potential and the quasi-Fermi level (E_f) are the same and very close to the lower edge of the conduction

band [35]. At potentials negative of the flat band potential for an n-type semiconductor, there is now an excess of the majority charge carrier (electrons) in the space charge region, which is referred to as an accumulation region.

Kandiel *et al*. [36] calculated the flat-band potentials of anatase and brookite by impedance spectroscopy using electrodes obtained by spreading the corresponding suspensions on conductive fluorine-tin oxide glasses. The quasi-Fermi levels (E_f) were, furthermore, obtained under UV illumination by the slurry method. The E_{FB} values estimated at pH 7 versus NHE were −0.35 eV for anatase and –0.54 eV for brookite whereas the corresponding E_f values were −0.68 eV and −0.77 eV respectively. The differences between these values were attributed to the independent methods performed under dark and illuminated conditions. The conduction band edges of anatase and brookite were calculated as the mean value of E_{FB} and E_f, i.e., −0.51 eV for anatase and −0.65 eV for brookite.

2.2 Crystal Structures and Doping with Transition Metals in TiO_2

2.2.1 Density Functional Theory Studies on TiO_2 Doping

In recent years, nano-sized TiO_2 powders have been used as a working electrode for dye-sensitized solar cells due to a higher efficiency than any other metal oxide semiconductor. However, it has been reported that the best TiO_2 solar cell efficiency could hardly reach 10.5 % [37]. First-principles computer simulations contribute to a deeper understanding of the dye/semiconductor interface lying at the heart of DSSCs. The study presented the results of simulation of dye adsorption onto rutile/anatase TiO_2 surfaces, and of their implications for the functioning of the corresponding solar cells [37].

In 2005 Park *et al*. [39] investigated the structure related to photocatalytic properties of TiO_2 and reported the band structures and the densities of states at the Fermi energy for rutile, anatase and brookite phases along with the structure-photocatalytic relationship using the first principle method based on DFT method. It was found that the band structures are less dispersive in anatase phase than in rutile phase, and they are almost flat in brookite phase. As a result, the density of states (DOS) value near the Fermi energy for brookite is highest among the three types of TiO_2, implying the number of electrons near the Fermi energy are largest in brookite. The calculations

that brookite phase may exhibit highest photocatalytic efficiency among other phases of TiO_2 [39].

In 2012 Hanaor *et al*. [40] investigated the phase stability of doped TiO_2 using the *ab-initio* density functional theory calculations of the relative stability of anatase and rutile polymorphs of TiO_2, carried out using all-electron atomic orbitals methods within local density approximation (LDA). They reported that the rutile phase exhibited a moderate margin of stability of ~ 3 meV relative to the anatase phase in the pristine material. Computational analysis of the formation energies of Si, Al, Fe and F dopants of various charge states across different Fermi level energies in anatase and rutile, showed that the cationic dopants are most stable in Ti substitutional lattice positions while formation energy is minimised for F doping in interstitial positions [40]. All dopants were found to considerably stabilize anatase relative to the rutile phase, suggesting the anatase to rutile phase transformation is inhibited in such systems with the dopants ranking F>Si>Fe>Al in the order of anatase stabilization strength. Al and Fe dopants were found to act as shallow acceptors with charge compensation achieved through the formation of mobile carriers rather than the formation of anion vacancies [40].

In 2013 Feng *et al*. [46] designed a series of metal-free donor-π-bridge molecules (denoted VB0–VB4) based on a new donor group—Ulla zine donor—as sensitizers for dye-sensitized solar cell applications. With the use of the first principles, density functional theory and time-dependent DFT calculations; it was revealed that the physical properties of dyes, including spectral response, light harvesting efficiency, and electron injection rate, are systematically improved by combining Ulla zine donor to a series of length changing π bridges. Dye VB2 was found to be the best candidate because of its outstanding performance on key parameters and achieving a balance between competing factors. Compared to two other series of molecules—L and M dyes, which differ from VB dyes by only the donor group—VB dyes have the largest light harvesting efficiency and the largest number of electrons injected to the conduction band of TiO_2. These results suggest that the Ulla zine group can serve as an excellent donor for future DSSCs applications [46].

Over the years there have been numerous investigations reported on the effective method to add group VIII metals to TiO_2-based photocatalytic systems to enhance the photocatalytic reaction rate [42-45]. In previous studies, one of the most active metals

for photocatalytic enhancement was platinum (Pt), which produced the highest Schottky barrier among the metals that facilitate electron capture [44]. The capture of electrons by Pt is postulated to produce a longer electron–hole pair separation lifetime, and therefore hinder the recombination of electron–hole pairs and enhance the transfer of holes and possibly electrons to O_2 adsorbed on the TiO_2 surface. Afterwards, excited electrons migrate to the metal, where they become trapped and the electron–hole pair recombination is suppressed. Therefore, many investigations have reported the enhancement of photo activities in both liquid and gas phase's results from depositing Pt, although some recorded reverse effects [45].

There is limited literature on the effect of Pt deposition on the surface of TiO_2 by means of photo reduction on optical absorption capability. The photoactivity enhancement of Pt-modified TiO_2 cannot simply be attributed to the capture of electrons by Pt and the Schottky barrier in the Pt facilitating the electron capture. Some research focused on the interaction of Pt with TiO_2 surface, and the effect of Pt on chemical state of Ti, energy level, and interfacial charge transfer [42, 43].

2.3 Brookite TiO_2 Surfaces

The difficulty in preparing brookite that has both high purity and large surface area is probably one of the reasons for the limited work on its photocatalytic properties. In 2008 Li *et al*. [41] investigated different reactivities of TiO_2 polymorphs using density functional theory calculations, comparing water and formic acid adsorption on anatase and brookite TiO_2 surfaces. The study illustrated that the brookite TiO_2 (210) has the same structural building block as anatase TiO_2 (101), but interatomic distances are slightly shorter and the blocks are arranged in a different way. Their calculations showed that these differences significantly change the reactivity toward adsorption of various molecules, and most importantly, generate highly active sites at the junction between different structural units on brookite TiO_2 (210). It further suggested that brookite TiO_2 (210) surface exhibits distinct activity, which may be useful in catalytic and photocatalytic applications.

In 2007 Finazzi *et al*. [47] investigated the incorporation of nitrogen impurities onto anatase TiO_2 (101) surface by first principles DFT calculations. The study considered several substitutional, interstitial configurations and different concentrations of

nitrogen impurities on the surface and subsurface layers, as well as their interactions with oxygen vacancies in the TiO_2 lattice. Also, the stability of the various systems on the basis of their formation energy as a function of the oxygen chemical potential were compared, which determined whether the system is in an oxidizing or reducing environment. The findings showed that under oxygen-rich conditions, N bound to a surface O is preferred, whereas, under oxygen-poor conditions, substitutional N together with oxygen vacancies is favoured, as previously found for bulk TiO_2. The cost of formation of a surface oxygen vacancy is almost cancelled in the presence of N impurities in subsurface layers. The incorporation of nitrogen in the lattice modifies the electronic structure by introducing localized states in the bandgap, consistent with experimentally observed surface absorption of N-doped anatase samples in the visible region. Also, these N impurity states are excellent traps for the Ti^{3+} electrons derived from surface oxygens vacancies [47].

In 2009 Chen *et al*. [48] used the DFT plane-wave pseudopotential method to investigate TiO_2 anatase (101) surfacess doped with oxygen vacancies and nitrogen atoms. The results demonstrated that the nitrogen doping is likely to reduce the bridging oxygen vacancy formation energy also the cost of substitution of the oxygen atoms with nitrogen atoms is reduced in the presence of oxygen vacancies. Moreover, the nitrogen doping has little effect on the defective surface restructuring. The results confirmed that the mixing of N dopants induced states with original Ti 3d and O 2p valence band attributed to the band gap narrowing [48].

Yang *et al*. [49] reported the investigation on TiO_2 (101) surface using the plane-wave ultrasoft pseudopotential method based on the density functional theory, with emphasis on the surface energy, band structure, density of states, and charge population. The anatase TiO_2 (101) crystal surface structure, whose outermost and second layers were terminated by two-fold coordinated oxygen atoms and five-fold coordinated titanium atoms, was found to be much more stable. The surface energy of the 18-layer atoms model was 0.580 J/m^2. The surface electronic structure was similar to that of the bulk with no surface state. Compared with the bulk structure, the band gap increased by 0.36 eV from 2.80 eV, the Ti_{5c}-O_{2c} bond lengths reduced to 0.171 Å after relaxation, and the charges of the surface were transferred to the body. Their analysis of the optical properties of the TiO_2 (101) anatase surface showed that

the system did not absorb in the low-energy region and an absorption edge in the ultraviolet region corresponding to the energy of 3.06 eV [49].

Kogo *et al*. [50] investigated a systematic representation of the adsorption behaviour of the highly efficient Ru (II) sensitizer (N3) on the anatase TiO_2 (001) surface based on density functional theory and found that three preferable configurations can be formed by exploiting two or three carboxylic groups attached to the TiO_2 surface, with their adsorption energies differing slightly. The interplay of N3 with the (001) surface is considerably stronger than that of N3 with the (101) surface, resulting in a larger dye coverage on the (001) surface. The energy gap of the N3 sensitizer determining the absorption spectrum, decreased by about 0.12 eV upon adsorption, suggesting an even larger range of the absorption spectrum than for the isolated N3 molecule. Moreover, the higher conduction band minimum of the TiO_2 (001) surface with N3 adsorption, compared with that of the (101) surface, indicates the higher open circuit potential. These results provide a clue on understanding the high solar light-to-electricity conversion efficiency of dye-sensitized solar cells with TiO_2 nanocrystals exposing a high percentage of (001) faces [50]

The recently, standard density functional theory calculations showed that brookite and rutile had direct band gaps of 1.86 eV and 1.88 eV, respectively, whereas an indirect band gap of 1.94 eV was observed for anatase [51]. Through the implementation of more modern approximation, the band gap underestimation was corrected and the E_g values of brookite, rutile and anatase were increased to 3.30 eV, 3.39 eV and 3.60 eV, respectively [51]. However, there is not much research on the optical properties of brookite TiO_2 (100), (010) and (210) surfaces. The study provide the fundamental theoretical data on structural, electronic and optical properties of the brookite TiO_2 (100), (010) and (210) surfaces doped with Ru and Pt using first-principle calculations. In particular, analyses of geometrical structure (bond lengths, bond angles, lattice parameters, etc.), surface properties, electronic properties (band gap, nature of bonding, electronic populations, etc.) and optical properties are presented.

CHAPTER 3

3.1 Methodology

3.1.1 Density Functional Theory

Density functional theory (DFT) is a computational quantum mechanical modelling method used in physics, chemistry and materials science to investigate the electronic structure (principally the ground state) of many-body systems, in particular atoms, molecules, and the condensed phases. It also derives properties of the molecule based on a determination of the electron of the molecule. DFT is based on the idea that all the ground state properties of the system of interacting particles can be derived from the ground state electron density $n_o(r)$ of the system. The theory is based on the concepts proposed by Thomas in 1927 [52] and Fermi in 1927 [53]. The original Thomas-Fermi method approximated the kinetic energy of the system as an explicit functional of the density, simplified as non-interacting electrons inhomogeneous gas. This homogenous electron gas is supposed to have a density equal to the local density at any given point. In this approximation, the exchange and correlation among the electrons were neglected, but this was later implemented by Dirac. The functional for energy in the case of electrons in an external potential $V_{ext}(r)$ is given as [52, 53]

$$E_{TF}[n] = \left(\frac{3(3\pi^2)^{\frac{2}{3}}}{10}\right)\int d^3 r n(r)^{\frac{5}{3}} + \int d^3 r \mathrm{V}_{ext}(r) n(r) + \left(-\frac{3}{4}\left(\frac{3}{\pi}\right)^{\frac{1}{3}}\right)\int d^3 r n(r)^{\frac{4}{3}} + \frac{1}{2}\int d^3 r d^3 r' \frac{n(r) n(r')}{|r - r'|} \tag{3.1}$$

In equation 3.1 the first term is the local approximation of the kinetic energy. The ground state of the system can be found by minimizing the $E[n]$ or all n(**r**). This original Thomas-Fermi method is a fine example of how the DFT works, but it is far too inaccurate for present day electronic structure calculations [52, 53].

The modern DFT is based on the theorems of Hohenberg and Kohn [54]. These theorems formulate DFT as an exact theory of many-body systems and are stated as:

- **Theorem 1:** For a system of interacting particles in an external potential, the external potential $V_{ext}(r)$ is uniquely determined by the ground state density $E[n]$ [51].

- **Theorem 2:** For any external potential $V_{ext}(r)$, the universal functional for energy $E[n]$ can be determine in terms of density n(**r**), and the global minimum for $E[n]$ as a function of n(**r**), which represents the exact ground state and the ground state density of the system [51].

Based on these two theorems, the energy functional can be formulated as:

$$E_{HK} = T[n] + E_{int}[n] + \int d^3 r V_{ext}(r) n(r) + E_{II}. \quad (3.2)$$

In equation 3.2, T[n] is the internal kinetic energy of the system, $E_{int}[n]$ is the internal potential energy, and E_{II} represents the interaction energy of the nuclei.

The reason for DFT to be the most used method for electronic structure calculations today is the Kohn-Sham ansatz introduced in 1965. Kohn and Sham stated that, the complicated many-body problem can be replaced with an auxiliary independent-particle problem, which can be solved far more easily. The Kohn-Sham method is self-consistent, dealing with independent particles and interacting density.

The famous Kohn-Sham ansatz is based on two assumptions:

- The exact ground state of the system can be represented by the ground state of the auxiliary system of non-interacting particles.

- The auxiliary Hamiltonian can be selected so, that it has a usual kinetic energy operator and an effective local potential $V_{eff}^{\sigma}(r)$, which acts on the electron in the point **r**, having a spin off σ [54].

3.1.2 Local Density Approximation

The local density approximation (LDA) is known to be the simplest method of describing the exchange correlation energy of an electronic system, which is widely used in total-energy pseudopotential calculations. LDA gives the correct sum rule for the exchange correlation hole. In the LDA it is assumed that the exchange-correlation energy depends only on the local electron density around each volume element dr. Using this approximation the exchange-correlation energy at point r for a density n(**r**) is equal to the exchange correlation energy per electron in a homogenous gas that has the same density as the electron gas and is given by [55-60]:

$$E_{xc}^{LDA} = \int \mathrm{n(r)} \in_{xc} (\mathrm{n})\, \mathrm{dr} \tag{3.3}$$

where $\in_{xc} (\mathrm{n})$ is the exchange-correlation energy per particle of uniform electron gas of density n. The extension of density functionals to spin-polarized systems is straight forward for exchange, where the exact spin-scaling is known, but for correlation further approximations must be employed. A spin polarized system in DFT employs two spin-densities, n_α and n_β. The form of the local-spin-density approximation (LSDA) is given by:

$$E_{xc}^{LSDA} = \int \mathrm{drn(r)} \in_{xc} (\mathrm{n}_\alpha, \mathrm{n}_\beta) \tag{3.4}$$

Despite the remarkable success associated with the LDA, it has some limitations. For systems where the density varies slowly, the LDA tends to perform well, and chemical trends are well reproduced. However, two systematic trends have been found in LDA, that is; the weak bonds are too short and the calculated binding energies are typically too large [57, 60].

3.2 Generalized Gradient Approximation

Beyond the LDA the exchange and correlation in an inhomogeneous system is non-local with respect to electrons it surrounds, and this is referred to as gradient correction. The terms in the exchange-correlation expression depend on the gradient of the electron density and not only on the value at each point in space. Generalized gradient approximation (GGA) was introduced by Perdew and Wang [60-63].

Generalized gradient approximations are still local but also take into account the gradient of the density at the same coordinate as the new variable. The GGA exchange energy is given by [63]:

$$E_x^{GGA}\,\mathrm{c(n)} = \int drn(\mathrm{r}) \in_{xc} \left[\mathrm{n(r)}, \|\nabla\,\mathrm{n(r)}\|\right] \tag{3.5}$$

where $\in_{xc}$ is the exchange correlation energy and $n(\mathrm{r})$ is the gradient term. GGAs tend to improve total energies, atomization energies, energy barriers and structural energy differences. It also expands and soften bonds, an effect that sometimes corrects and sometimes overcorrects the local spin density approximation. The GGA functional are most commonly used in physics.

3.3 Plane-Wave Pseudopotential Method

The plane-wave pseudopotential method has become a powerful and reliable tool to study the properties of a broad class of materials. The emphasis on the total energy and the related properties makes plane-wave pseudopotential a technique suitable for structural studies based on a quantum-mechanical treatment of the electronic subsystems. The main idea of the method is to simplify the DFT problem by considering only valence electrons. Core electrons are excluded under the assumption that their charge density is not affected by the changes in the chemical environment. This approximation is well understood and gives a number of computational advantages such that [64]:

- The pseudopotential is much weaker in the core region than the true Coulomb potential of the nucleus, and it does not have a singularity at the position of the nucleus.
- The resulting pseudo-wave functions are smooth and nodeless in the core region.
- There are fewer electronic states in the solid-state calculations.
- Both pseudopotentials and pseudo-wave functions can be efficiently represented using a plane wave basis set.

The plane wave pseudopotential method is applicable to large systems that are subjected to 3D periodic boundary conditions.

3.2.1 Plane-Wave Basis

As yet there has been no mention of how to handle the infinite number of interacting electrons moving in the static field of an infinite number of ions. Essentially, there are two difficulties to overcome: a wave function has to be calculated for each of the infinite number of electrons, which will extend over the entire space of the solid and the basis set in which the wave function expressed will be infinite. Bloch's theorem uses the periodicity of a crystal to reduce the infinite number of one-electron wave functions to be calculated and to simply the number of electrons in the unit cell of the crystal (or half that number if the electronic orbitals are assumed to be doubly occupied - that is, spin degenerate). The wave function is written as the product of a cell periodic part and a wavelike part [63]:

$$\Psi_{ki}(r) = exp[ik.r]\, f_i(r) \tag{3.6}$$

The first term is the wavelike part which will be discussed below. The second term is the cell periodic part of the wave function. This can be expressed by expanding it into a finite number of plane waves whose wave vectors are reciprocal lattice vectors of the crystal, given by [63]:

$$f_i(r) = \sum_G G_{i,G} exp[iG.r] \tag{3.7}$$

where G represents reciprocal lattice vectors given by $G.\mathrm{I} = 2\pi\,\mathrm{m}$ for I, where I is a lattice of the crystal and m is an integer. Thus, each electronic wave function can be written as a sum of plane waves such that:

$$\Psi_{ki}(r) = \sum_G G_{i,k+G}\left[i(\mathrm{k}+G).\mathrm{r}\right] \tag{3.8}$$

where $G_{i,k+G}$, the coefficients for the plane are waves that need to be solved and depend entirely on the specific kinetic energy, $\left(\frac{h^2}{2m}\right)|k+G|^2$.

The convergence of this expansion is controlled by the choice of the kinetic energy cut-off, since the plane waves with a smaller kinetic energy typically have a more important role than those with a very high kinetic energy. The introduction of a plane wave energy cut-off reduces the basis set to a finite size. This kinetic energy cut-off will lead to an error in the total energy of the system but in principle it is possible to make this error arbitrarily small by increasing the size of the basis set by allowing a larger energy cut-off. The cut-off that is used in practice depends on the system under investigation.

The plane-waves are used as a basis set for the electronic wave functions, and substitution of equation 3.6 into equation 3.8 leads to:

$$\left\{\frac{\hbar^2}{2m}\nabla^2 + V(\mathrm{r})\right\}\varphi_i(\mathrm{r}) = \mathrm{c}_\mathrm{i}\,\varphi_i(\mathrm{r}) \tag{3.8}$$

the integration over r gives the following secular equation:

$$\sum_{G'}\left[\frac{h^2}{2m}\left|k+G\right|^2\delta_{GG'} + V_{ion}(\mathrm{G}-\mathrm{G}') + V_H(\mathrm{G}-\mathrm{G}')\right]C_{i,k+G'} = \varepsilon_i C_{i,k+G} \tag{3.9}$$

It is noted that the first contribution, the kinetic energy, is diagonal whereas the various potential contributions are given by their Fourier transforms. This may be written in terms of the Hamiltonian matrix elements $H_{k+G,k+G'}$ as:

$$\sum_{G'} H_{k+G,\mathrm{k}+G'}C_{i,k+G'} = \varepsilon_i C_{i,k+G'}. \tag{3.10}$$

The solutions of the Kohn-Sham equation are obtained by diagonalizing the Hamiltonian matrix elements $H_{k+G,k+G'}$. The size of these matrix elements is determined by the choice of energy cut-off $\left(\frac{h^2}{2m}\right)\left|k+G\right|^2$, and will be large for systems that contain both valence and core electrons.

Although Bloch's theorem states that the electronic wave functions can be expanded using a discrete set of plane waves, a plane wave basis set is usually very poorly suited to expanding electronic wave functions because a very large number of plane

waves are needed to expand the tightly bound core orbitals and to follow the rapid oscillation of the wave functions of the valence electrons in the core region. An extremely large plane wave basis set would be required to perform all electron calculations, and a vast amount of computational time would be required to calculate the electronic wave functions. This problem can be overcome by the use of pseudopotential approximation [63-66].

3.2.2 Pseudopotential Method

Pseudopotential or effective potential in physics is used as an approximation for the simplified description of complex systems. Applications include atomic physics and neutron scattering. The pseudopotential approximation was first introduced by Hans Hellmann in 1933 [67]. The pseudopotential is an attempt to replace the complicated effects of the motion of the core (i.e. non-valence) electrons of an atom and its nucleus with an effective potential, or pseudopotential, so that the Schrödinger equation contains a modified effective potential term instead of the Coulombic potential term for core electrons normally found in the Schrödinger equation. Figure 3.1 illustrates the ionic potential $\left(Z/r\right)$, the valence wave function $\left(\psi_v\right)$, the corresponding pseudopotential $\left(V_{pseudo}\right)$, and pseudo-wave function $\left(\psi_{pseudo}\right)$ respectively [65]. The pseudopotential is an effective potential constructed to replace the atomic all-electron potential (full-potential) such that core states are eliminated and the valence electrons are described by pseudowave functions with significantly fewer nodes. This allows the pseudowave functions to be described with far fewer Fourier modes, thus making plane-wave basis sets practical to use. In this approach usually only the chemically active valence electrons are dealt with explicitly, while the core electrons are 'frozen', being considered together with the nuclei as rigid non-polarizable ion cores. It is possible to self-consistently update the pseudopotential with the chemical environment that it is embedded in, having the effect of relaxing the frozen core approximation, although this is rarely done. First-principles pseudopotentials are derived from an atomic reference state, requiring that the pseudo- and all-electron valence eigenstates have the same energies and amplitude (and thus density) outside a chosen core cut-off radius r. Pseudopotentials with larger cut-off radius are said to be softer, that is more rapidly convergent, but at

the same time less transferable, that is less accurate to reproduce realistic features in different environments. Without any doubt the pseudopotential approximation is the most widely used method in electronic structure theory dealing with heavy atoms where relativistic effects need to be considered. Pseudopotential calculations are less accurate than all-electron calculations, but they simulate the results of the latter often surprisingly well, for substantially smaller expenses.

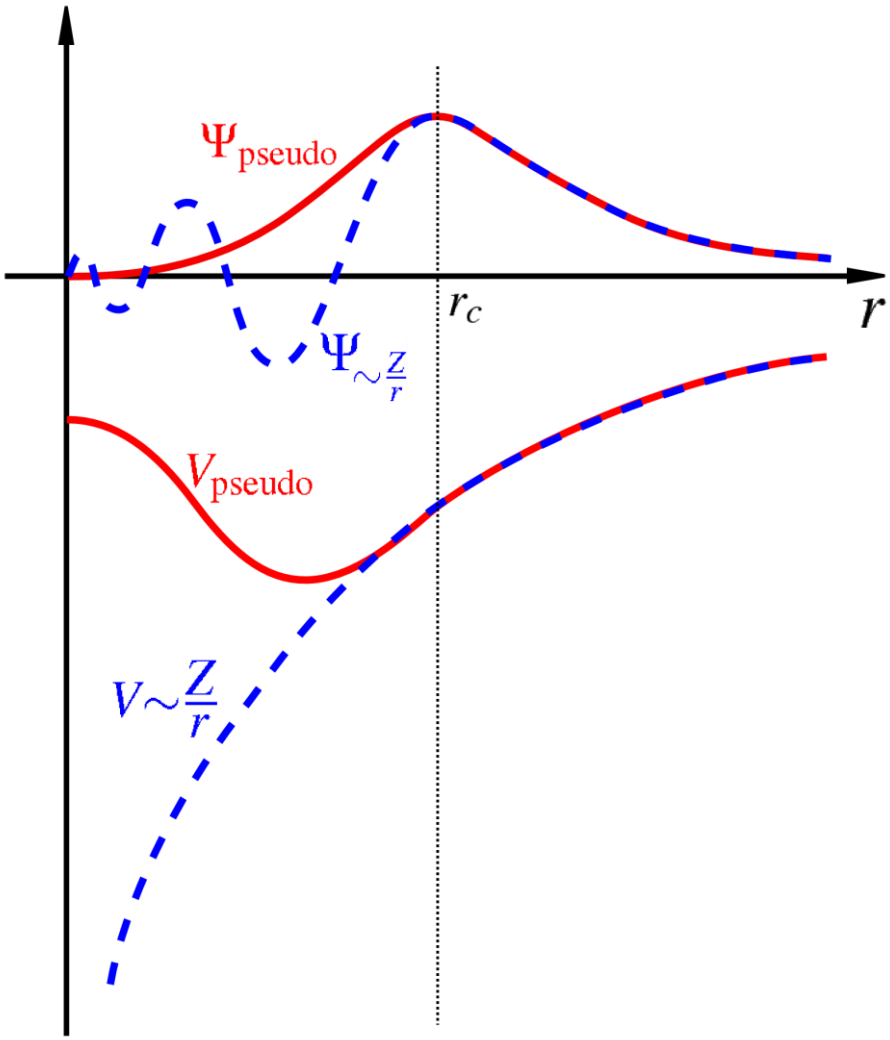

Figure 3. 1 Comparison of a wave function in the Coulomb potential of the nucleus (blue) to the one in the pseudopotential (red). The real and the pseudo wave functions and potentials match above a certain cut-off radius r_c [68].

The advantage of using the pseudopotential approximation is that it allows the electronic wave function to be expanded using a much smaller number of plane wave basis states, so that a smaller amount of computational time would be required for convergence of the energies. The pseudopotential takes the form:

$$V_{NL} = \sum_{lm} |lm\rangle V_l \langle lm|, \tag{3.11}$$

where $|lm\rangle$ is the spherical harmonics and V_l is the pseudopotential for angular momentum l. The majority of the pseudopotential currently used in the electronic structure is generated from all electron atomic calculations.

A pseudopotential that uses the same potential for all the angular momentum components of the wave function is called a local pseudopotential. A local pseudopotential is a function that only depends on the distance dependence of the potential. The norm-conserving pseudopotential (NCP) by Kleinmann and Bylander [69] is an example of a non-local pseudopotential, using a different potential for each angular momentum component of the wave function. Recently, the ultrasoft pseudopotential (USP) put forward by Vanderbilt [67] has been implemented in plane-wave calculations. In this scheme, the pseudo wave functions can be as soft as possible within the core region. They cover a wide range of atoms, including the transition metals. In this dissertation, ultrasoft pseudopotential by Vanderbilt [67] within the Cambridge Serial Total Energy Package (CASTEP) code [68, 69] for total energy calculations were used since they give accurate results for the system under investigation.

3.4 Cambridge Serial Total Energy Package

CASTEP is premier density functional theory quantum mechanical code used to simulate the properties of solids, interfaces, and the surfaces for a wide range of materials classes including ceramics, semiconductors and metals [72]. CASTEP employs plane-wave techniques to deal with materials with weak pseudopotentials. First principle calculations allow researchers to investigate the nature and the origin of the electronic, optical and structural properties of a system without the need for any experimental input, with the exception of the atomic number of mass of the constituent atoms.

CASTEP is well suited to research problems in solid state physics, materials science, chemistry and chemical engineering. In these fields, researchers can employ computer simulations to perform virtual experiments, which can lead to tremendous

results. This method can calculate forces acting on atoms and stress on the unit cell. CASTEP relies on a plane wave basis, pseudopotentials and the use of density functional theory to describe the valence electrons in a model. Other ingredients include fast Fourier transforms and minimization of the total energy rather than matrix diagonalization. In this study CASTEP code was used to perform all the calculations. The schematic representation in Figure 3.6 shows a summary of SCF methods for geometry optimization calculations DFT.

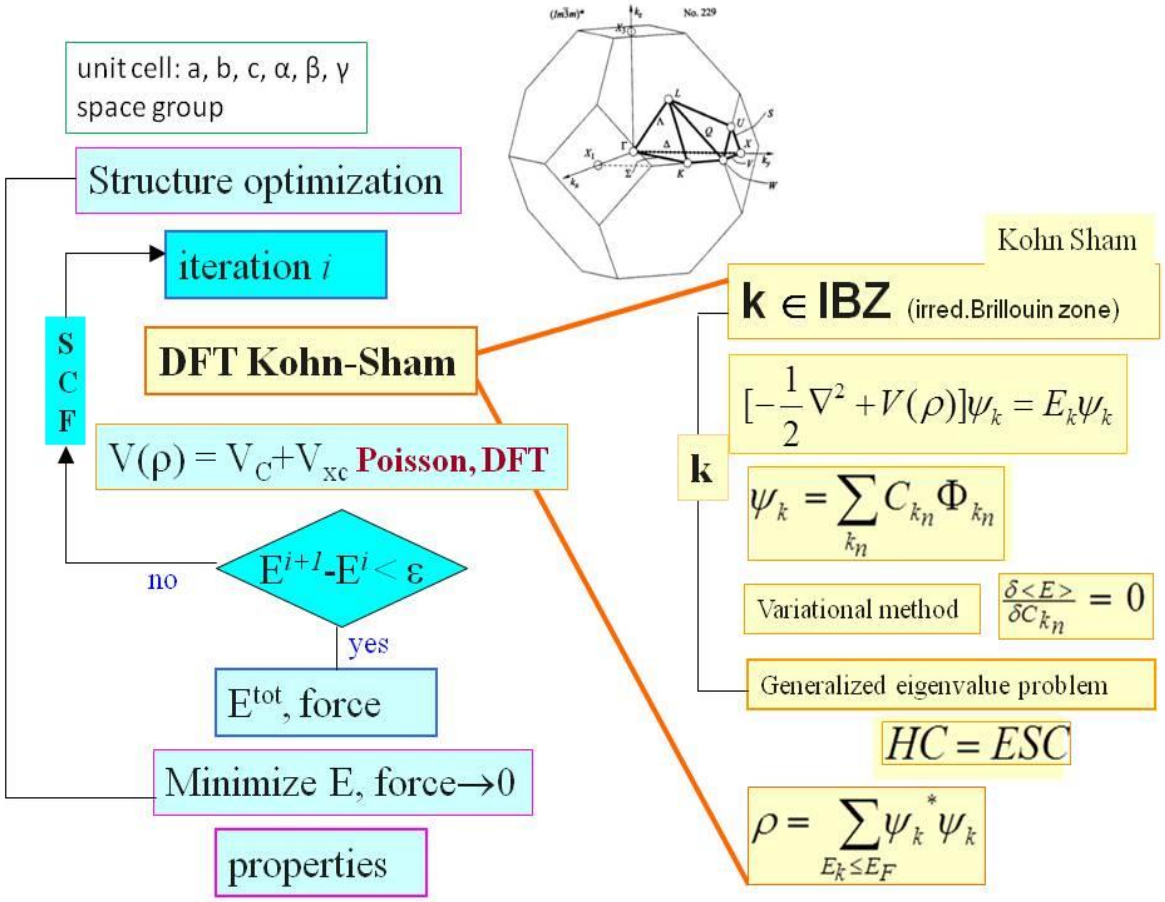

Figure 3. 2 Schematic representation of SCF and geometry optimization methods used in DFT [71].

3.5 Convergence Tests

The tag KSPACING determines the number of k-points if the KPOINTS file is not present. KSPACING is the smallest allowed spacing between k-points in units of $Å^{-1}$. The number of k-points increases when the spacing is decreased. In the reciprocal mode, the k-points are given by:

$$\vec{k} = x_1\vec{b_1} + x_2\vec{b_2} + x_3\vec{b_3} \tag{3.12}$$

where $\vec{b}_{1...3}$ the three-reciprocal basis are vectors, and $x_{1...3}$ are the supplied values. In the Cartesian input format, the k-points are given by:

$$\vec{k} = \frac{2\pi}{a}(x_1, x_2, x_3) \tag{3.13}$$

The unit cell of a face-centred cubic lattice is spanned by the following basis vectors:

$$A = \begin{pmatrix} 0 & a/2 & a/2 \\ a/2 & 0 & a/2 \\ a/2 & a/2 & 0 \end{pmatrix} \tag{3.14}$$

And the reciprocal lattice is defined as the matrix

$$2\pi B = \begin{pmatrix} -1 & -1 & 1 \\ 1 & -1 & 1 \\ 1 & 1 & -1 \end{pmatrix} \tag{3.15}$$

Before any geometry optimization could be performed it is important to calculate the energy cut-off for system that will give expansion of the plane wave functions and total energy within the plane-wave pseudopotential. The importance of calculating energy cut-off and k-mesh is to get the good convergence of the total energy, however the number of k-points depend on the system. In this work, the Monkhorst and Pack scheme was used to determine suitable cut-off energy using the default k-points and varying the cut-off energy from 260 eV to 800 eV. Then the identified energy cut-off was used to determine suitable k-points for bulk brookite TiO_2.

3.6 Computational Details

The structural, electronic and optical properties of doped and un-doped TiO_2 (100), (110) and (210) surfaces were performed using first principles calculations based on DFT plane-wave pseudopotential method. The generalized gradient approximation in the scheme of Perdew-Burke-Ernzerhof (PBE) was used to describe the exchange-correlation functional. All calculations were carried out using CASTEP code in Materials Studio of BIOVIA Inc. The Brillouin zone k-point sampling was performed using a Monkhorst–Pack mesh, and the cut-off kinetic energy of plane waves was set to 650 eV. The convergence criteria for structural optimization were set to be medium quality with the tolerance for self-consistent field (SCF), energy, maximum force, and maximum displacement of 2.0106 eV/atom, 2.0105 eV/atom, 0.05 eV/Å and 2.0103 eV/Å, respectively. The surfaces were doped by replacing one Ti atom with Ru/Pt atom (substitutional doping).

CHAPTER 4

4 Results and Discussions

In this chapter results obtained from quantum-mechanical calculations as defined in density functional theory in the previous chapter are presented. Thus, theoretical study of structural, electronic and optical properties of undoped and Ru or Pt doped brookite TiO_2 surfaces are presented. Plane wave pseudopotential method as implemented in CASTEP code was used to perform all the calculations.

4.1 Convergence Tests

There are two parameters that affect the accuracy of density functional theory calculations, namely kinetic energy cut-off that determines the number of plane waves in the expansion and the k-points that are used for Brillouin zone integration. Therefore, it is inessential to ensure that the appropriate energy cut-off and k-points are used. To find convergence parameters for brookite TiO_2 system, the energy cut-off and k-points were varied as a function of total energy. The graphs of total energy against energy cut-off and k-points are shown in Figures 4.1 and 4.2 respectively.

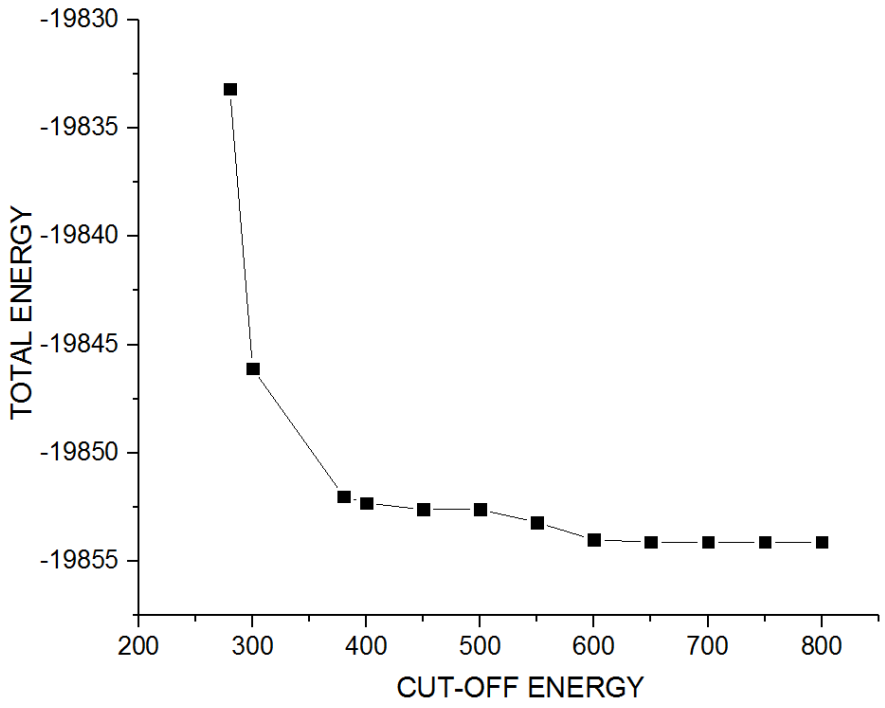

Figure 4. 1 Total energy against cut-off energy for bulk brookite TiO_2.

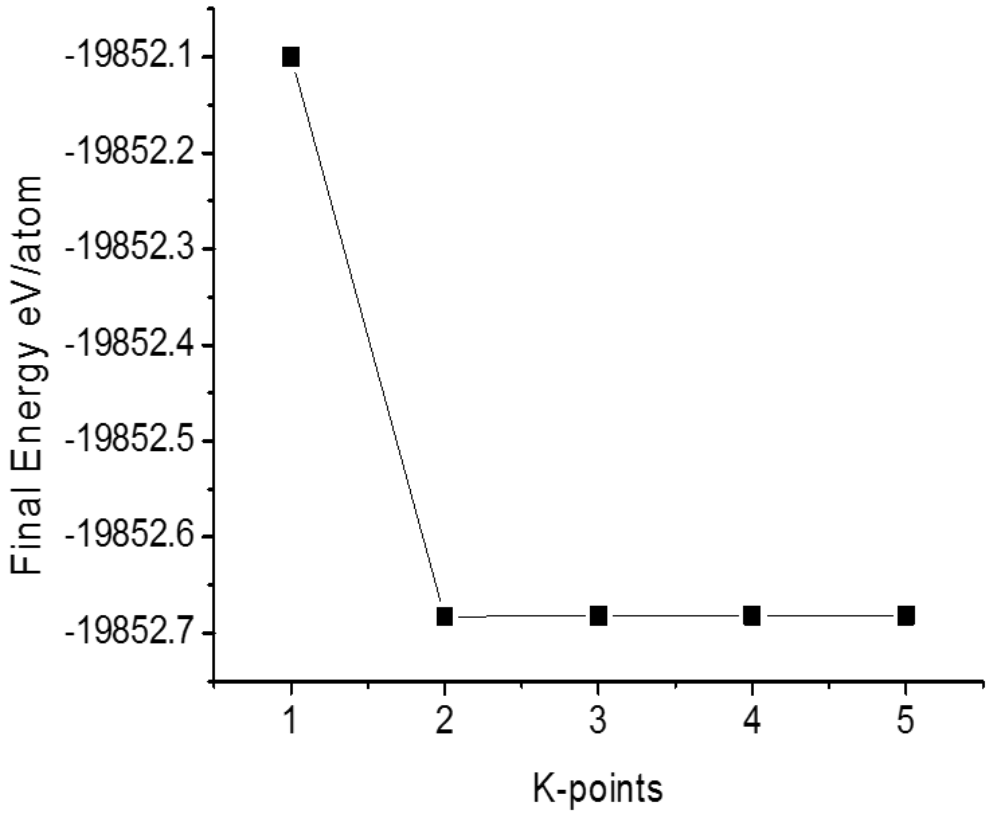

Figure 4. 2 Graph of final energy of formation vs the number of k-points for brookite TiO_2.

The kinetic energy cut-off is an important parameter in first principle calculations. Calculations of total energy versus energy cut-off were performed until a constant minimum energy was obtained. From the graph in Figure 4.1 it can be observed that from 600 eV, the energy becomes stable and the cut-off energy that corresponds to the minimum total energy can be obtained. Therefore, the cut-off energy of 650 eV was chosen and used throughout the calculations in the study. Pullay correction on forces was included to compensate the energy cut-off. The Monkhost-Pack scheme of the k-point scheme was used to select optimal set of special k-points of the Brillouin zone such that the greatest possible accuracy is achieved from the number of k-points used. The number of k-points was determined by computing self-consistent field calculations for different k-points. The total energy of the system as a function of k-points is shown in Figure 4.2. In this study, the least total energy was found to correspond to 4×4×2 k-points and was used to perform the geometry optimization of bulk brookite TiO_2.

4.2 Bulk Brookite-TiO_2

4.2.1 Structural Properties

Brookite is a member of the TiO_2 polymorphs family together with rutile and anatase. Brookite TiO_2 is known to have a complex structure, consisting of eight formula units in the orthorhombic cell (space group Pbca). The formation of brookite structure may be envisioned as the joining of distorted TiO_6 octahedral sharing three edges. Figure 4.3 illustrates the bulk structure of brookite TiO_2. Structural properties of a system require a calculation of the total energy of the system and subsequent minimization of that energy with respect to coordinates.

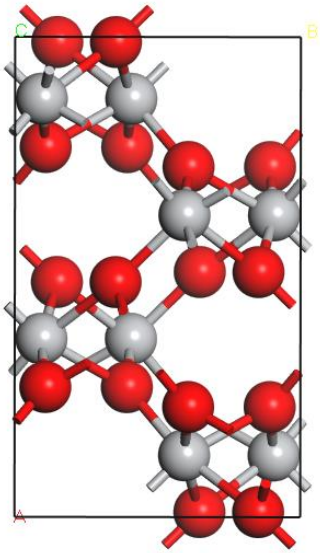

Figure 4. 3 The bulk structure of TiO_2 brookite. The grey spheres represent Ti atoms while red spheres represent O atoms.

Initially, brookite bulk system was geometrically optimized using generalized gradient approximation as implemented in density functional theory. The calculations were performed using the sets of k-points and energy cut-off evaluated through the convergence tests as described in section 4.1. Geometry optimizations were performed in one steps, with the unconstrained volume, to determine equilibrium bulk parameters and reference energies. These calculations on the bulk system were performed as a way of validating the accuracy of the model and the approximations used by comparing parameters with experimental values, before surface properties could be investigated.

The bulk structure of brookite TiO_2 was geometrically optimized to find the equilibrium lattice parameters with the lowest energy. Table 4.1 shows calculated lattice parameters against the reported experimental and previous theoretical results. The calculated results are in good agreement with both the experimental and reported theoretical results as reported in references [74, 75]. The obtained lattice parameters deviate from experimental data by 0.1967 % along the a-axis, 0.203 % along the b-axis and 0.196 % along the c-axis. In comparison with the previous theoretical results reported in [75], the calculated results are more accurate relative to experimental data, and thus validating the starting models and method used. Optimized fractional coordinates are in excellent agreement with the experimental values [74, 75] and are presented in Table 4.2. The results show that the atomic internal coordinates also vary isotopically at different positions. The theoretical determination of the stability and structure of materials under conditions that are difficult to reproduce in the laboratory is an added value of the present calculations.

Table 4. 1 Calculated lattice parameters for bulk brookite TiO_2 compared with experimental and previous theoretical results.

	Experimental [74]	Literature Calculations [75]	This work Calculations
Lattice Parameter			
a (Å)	9.184	9.157	9.166
b (Å)	5.447	5.430	5.436
c (Å)	5.145	5.122	5.135
Fractional coordinates			
Ti1	(0.129)(0.097)(-0.137)	(0.129)(0.091)(-0.146)	(0.127)(0.113)(-0.17)
O1	(0.010)(0.149)(0.182)	(0.011)(0.151)(0.180)	(0.010)(0.155)(0.180)
O2	(0.230)(0.113)(-0.463)	(0.230)(0.110)(-0.470)	(0.230)(0.105)(-0.465)

4.2.2 Electronic properties

Fundamentally the electronic properties of a system help in understanding the classification of a material categories, namely; metals, semiconductor and insulator. The type of the material is determined by the size and existence of the energy band gap between the conduction band and valence band. The band structure of brookite TiO_2 was constructed along the appropriate high-symmetry directions of the corresponding irreducible Brillouin zone using the calculated lattice parameters listed in Table 4.1. The calculated energy band gap of the bulk brookite TiO_2 was found to be 2.35 eV. The band gap value is consistent with the value reported by Mo and Ching [35] obtained using the self-consistent orthogonalized linear combination of atomic orbitals method. According to Mo and Ching [35] brookite TiO_2 had a direct band gap of 2.20 eV. Both the values were found to be underestimated compared with the experimentally measured value of 3.40 eV, this is due to the limitation of DFT method. The limitation is caused by the fact that the discontinuity in the exchange correlation potential which is not taken into account within the framework of DFT. However, the discussions on energy gap will not be affected because only the relative energy changes are of concern. In this work, the scissor operation of 1.047 eV was employed to compensate for the underestimation of the band gap [74].

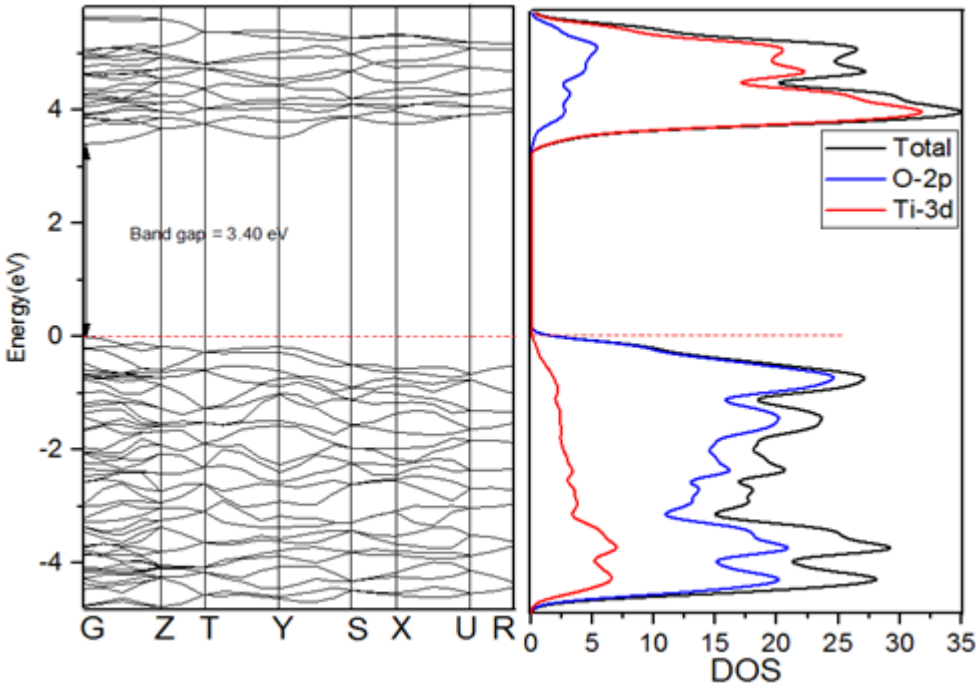

Figure 4. 4 Calculated band structure and density of states of bulk brookite TiO_2.

The scissors scheme aligns both the theoretical valence band energy (VBE) and conduction band energy (CBE) with their experimental counterparts, performing a "scissors" operation to stretch out the theoretical gap states over the experimental gap. The experimental value used for the scissor operation is 3.40 eV, which was reported by Koelsch, *et al.* [74] wherein brookite nanoparticles dispersed in water were investigated. After the scissor operation, the band gap value becomes 3.40 eV as shown in Figure 4.4. Both the conduction band minimum (CBM) and the valence band maximum (VBM) are located at G. Therefore, brookite TiO_2 is considered to be a direct band gap semiconductor. The upper valence band (VB) is lying in the range of 1.93-6.34 eV consisting of O 2p orbitals hybridized with Ti 3d orbitals. The bottom of the conduction band (CB) at -1.24 eV is composed of Ti 3d orbitals,

4.2.3 Optical Properties

The study of the optical functions of solids helps give a better understanding of optical properties for different materials. The frequency-dependent dielectric function is given by:

$$\varepsilon\left(\omega\right) = \varepsilon_1\left(\omega\right) + i\varepsilon_2(\omega) \tag{4.1}$$

The dielectric function is closely related to the electronic band structure. It fully describes the optical properties of any homogeneous medium at all photon energies. The imaginary part $\varepsilon_2\left(\omega\right)$ of the complex dielectric function is obtained from the momentum matrix elements between the occupied and unoccupied electronic states. The imaginary part is calculated using the analytical expression:

$$\varepsilon_2\left(\omega\right) = \frac{2e^2\pi}{\Omega\varepsilon_0}\sum_{k,v,c}\left|\left\langle\psi_k^c\left|\hat{u}\bullet\right.\right.\left[redacted\right]\left|\psi_k^v\right\rangle\right|^2\delta\left(E_k^c - E_k^v - E\right) \tag{4.2}$$

where ω is the frequency of light, e is the electronic charge, û is the vector defining the polarization of the incident electric field, ψ_k^c and ψ_k^v are the conduction and valence band wave functions at k, respectively. The real part of the dielectric function $\varepsilon_1\left(\omega\right)$ is derived from the imaginary part of the dielectric function $\varepsilon_2\left(\omega\right)$ through the Kramers–Kronig relations. Other optical properties, such as refractive index,

absorption spectrum, loss function, reflectivity, and conductivity (real part), are derived from:

$$\varepsilon_1(\omega) = 1 + \frac{2}{\pi} P \int_0^{\infty} \frac{\omega' \varepsilon_1(\omega') d\omega'}{(\omega'^2 - \omega^2)} \quad (4.3)$$

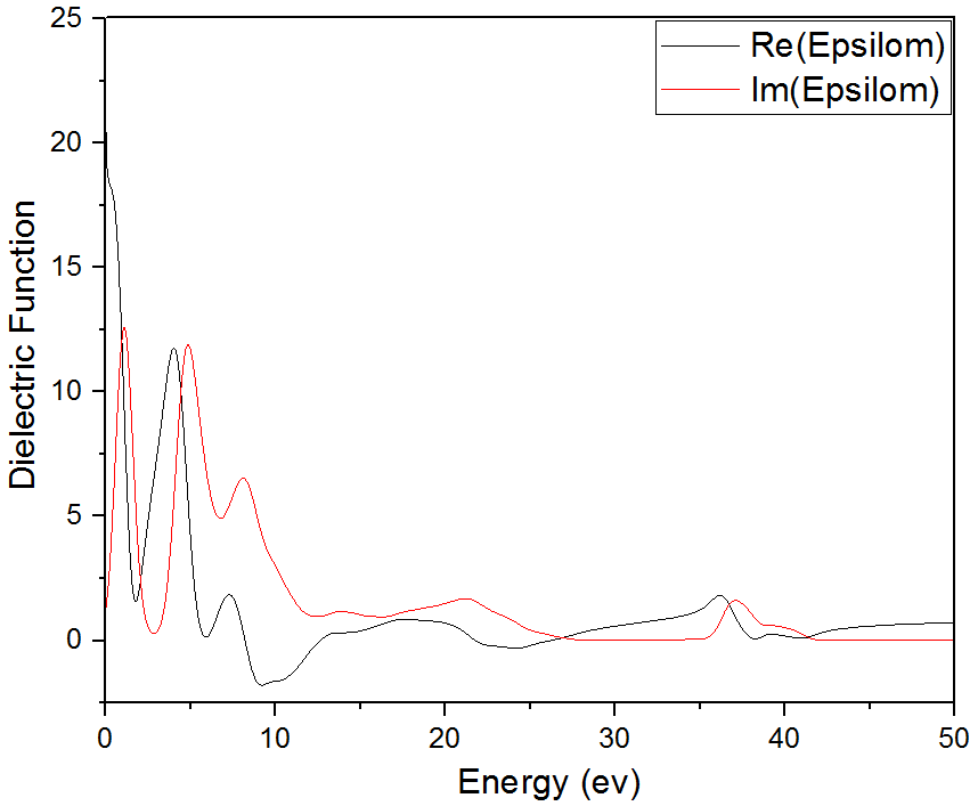

Figure 4. 5 Dielectric function of the bulk brookite TiO_2 structure showing the real and imaginary parts.

After geometrical optimization of the TiO_2 bulk structure, the real and imaginary parts of the dielectric function versus photon energy change were calculated and curve are shown in Figure 4.5. There are four peak positions in the imaginary part as shown in the graph. The first high and sharp peak appears at 1.2 eV because the valence band O 2p states jump to the conduction band Ti 3d states, according to analysis of the energy band diagram and density of states. The second, third, fourth and fifth peaks are at ~4.5 eV, ~8 eV, 21 eV and ~36 eV respectively, mainly owing to the electron transition from the O 2s state to the Ti 3d state. Currently, there are no literature results to compare the calculated properties, particularly for brookite TiO_2.

In this work, the optical absorption of bulk brookite TiO_2 was calculated. Again, scissor operation was considered in the calculations due to the underestimation of the bad gap by DFT, which makes it difficult to obtain the exact band gap together with the associated optical properties. This scissor operation can effectively describe the difference between the theoretical and experimental band gap values. From the calculated results in Figure 4.6, it can be observed that brookite bulk structure absorbs light in the ultra violet region. This is attributed by a high peaks ranging from 100 nm to 400 nm. The results suggest that the materials can be stable at wavelengths below 400 nm. Furthermore, bulk brookite TiO_2 also showed some long wavelength activity in the visible region. This can be observed by a peak between 500 nm and 1000 nm. These results show little activity of brookite in the visible region. Thus, the absorption of bulk brookite in the visible region is small compared to its absorption in the UV region, which may have some effects on solar cell performance.

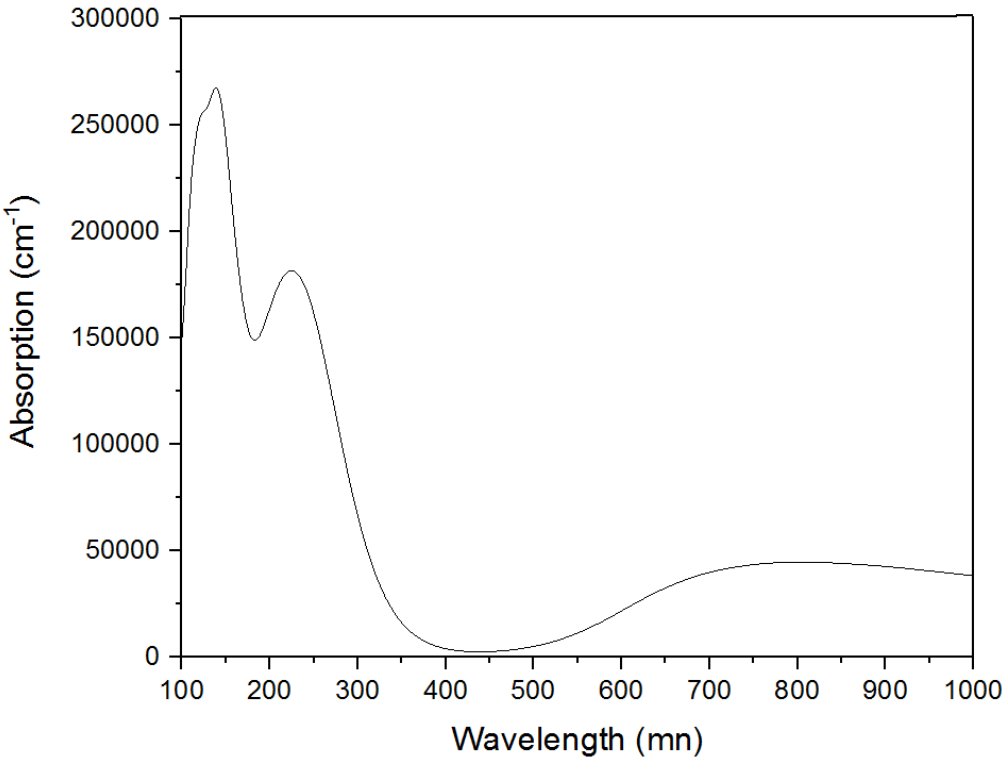

Figure 4. 6 Optical absorption curves of the bulk brookite TiO_2 structure.

The reflectivity is the ratio of a wave reflected from a surface of energy possessed by the wave striking the surface. The reflectivity spectra of bulk brookite TiO_2 is displayed in Figure 4.7 as a function of energy. The reflectivity is much higher in the infrared region with a starting higher value of ~0.44, which immediately decreases up to a value

of ~0.08, and then rises again to reach second maximum value of ~0.40 in the energy range of 0–6 eV. The reflectivity then rises again to reach a third maximum value of ~0.42 in the energy range of 6–10 eV, which concludes the first broad peak which constitutes of three splitting peaks. Two more peaks are observed at higher energies. With an increase in photon energy, the reflectivity graph is composed of several other peaks before falling rapidly to a lower value at the energy value of ~60 eV. A large reflectivity for E < 1 eV indicates the characteristics of high conductance in the low energy region. The energy loss spectrum describes the energy loss of electrons when passing through a uniform dielectric, and the energy loss peak describes the plasma resonance frequencies. The main energy loss for bulk brookite TiO_2 is at about ~25 eV and ~40 eV. Figures 4.7 and 4.8 reveal that the energy loss peaks for bulk brookite TiO_2 correspond to the sharp decline in the reflectivity spectrum.

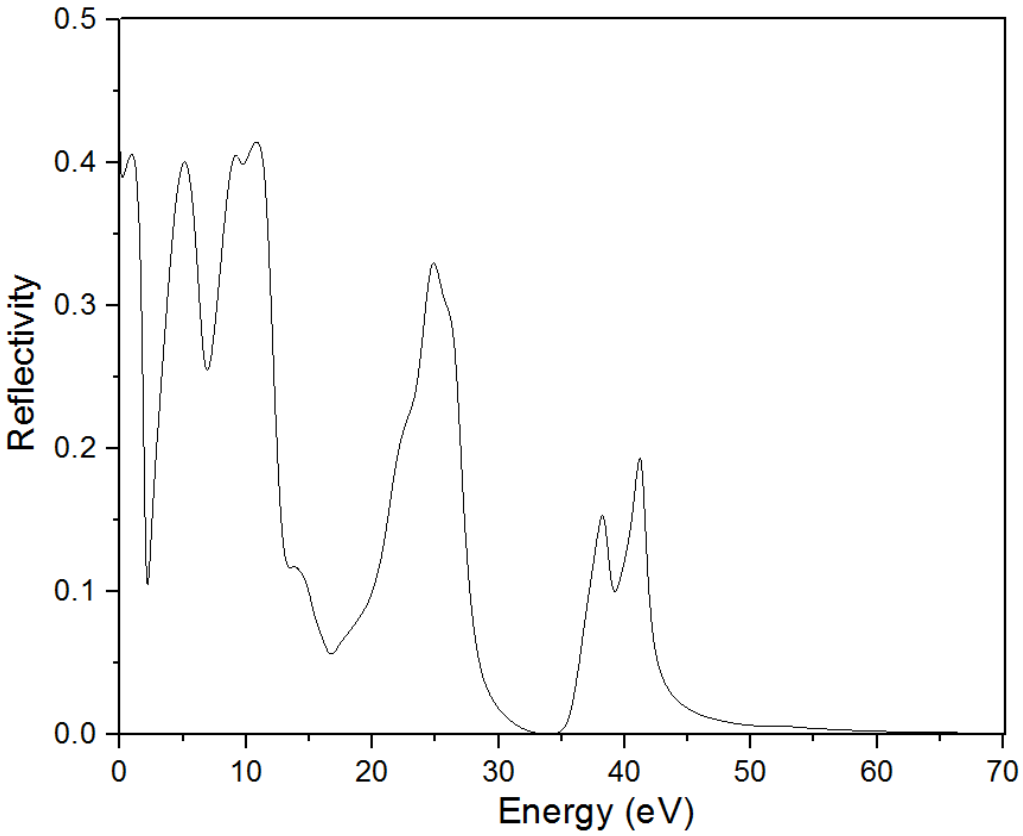

Figure 4. 7 Reflection spectrum of the bulk brookite TiO_2 structure.

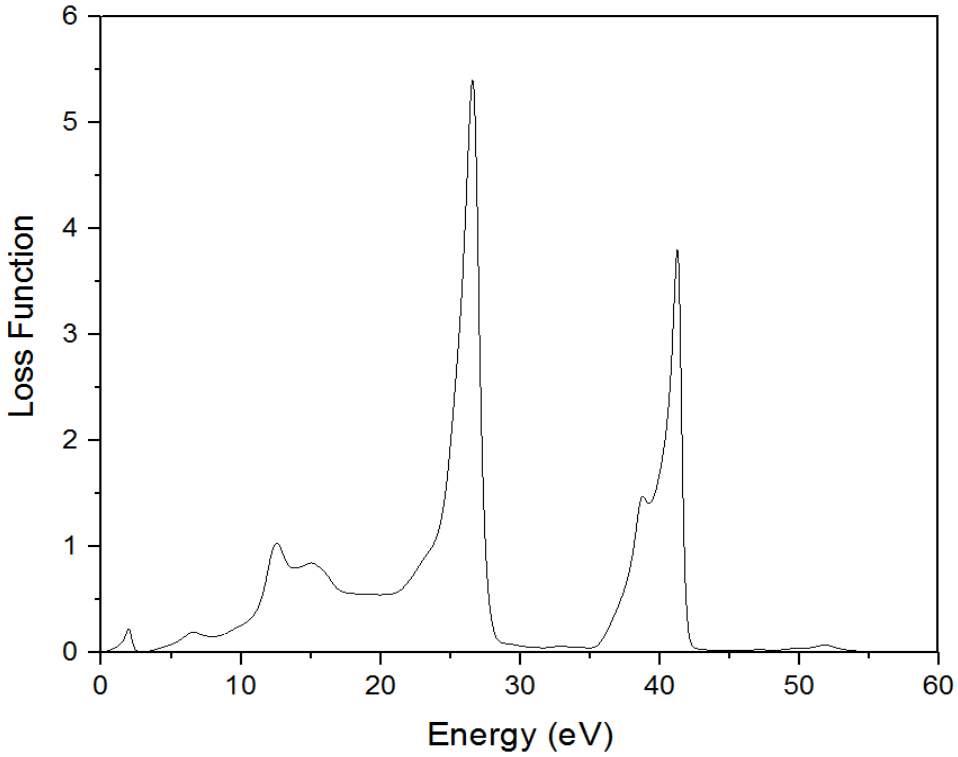

Figure 4. 8 Energy loss function of the bulk brookite TiO_2 structure.

4.3 Surfaces

4.3.1 Surface Properties

There are several methods available to model surfaces. For surface calculations, a bulk unit cell is cut in a specified orientation and duplicated via periodic boundary conditions in two dimensional. In this study, the surface structures of brookite have been created by cleaving a surface from the optimized bulk structure along a specified orientation and then built a slab. In this report, the selected three low index surfaces for brookite TiO_2 are investigated, i.e. (100), (110) and (210) surfaces are discussed. The surface structures of brookite have been modelled from unreconstructed (truncated bulk) slab models using the calculated equilibrium geometry. As these surfaces have different number of atoms in each layer, after the corresponding convergence tests, the low index surfaces were periodically modelled along *x*- and *y*-directions but with different thickness in the *z*-direction. The relaxation of these surfaces has been taken into account by optimizing all the layers of the slab.

4.3.1.1 (100) Surface

A schematic representation of the brookite (100) surface is depicted in Figure 4.9. The truncation of the octahedral renders different coordination combinations for the outermost titanium cations. Depending on the orientation of the brookite surface, the surface may be either oxygen- or titanium terminated. However, in this study the effect of surface termination is not investigated in detail as the focus was on understanding the effect of doping with Ru and Pt. The vacuum and crystal thickness used for the slabs are 10.0 Å and 19.05 Å, respectively. All the (100) brookite surface structures were optimized by relaxing surface atoms to eliminate surface atomic tension. The dopants were introduced by replacing one Ti atomice with Ru or Pt.

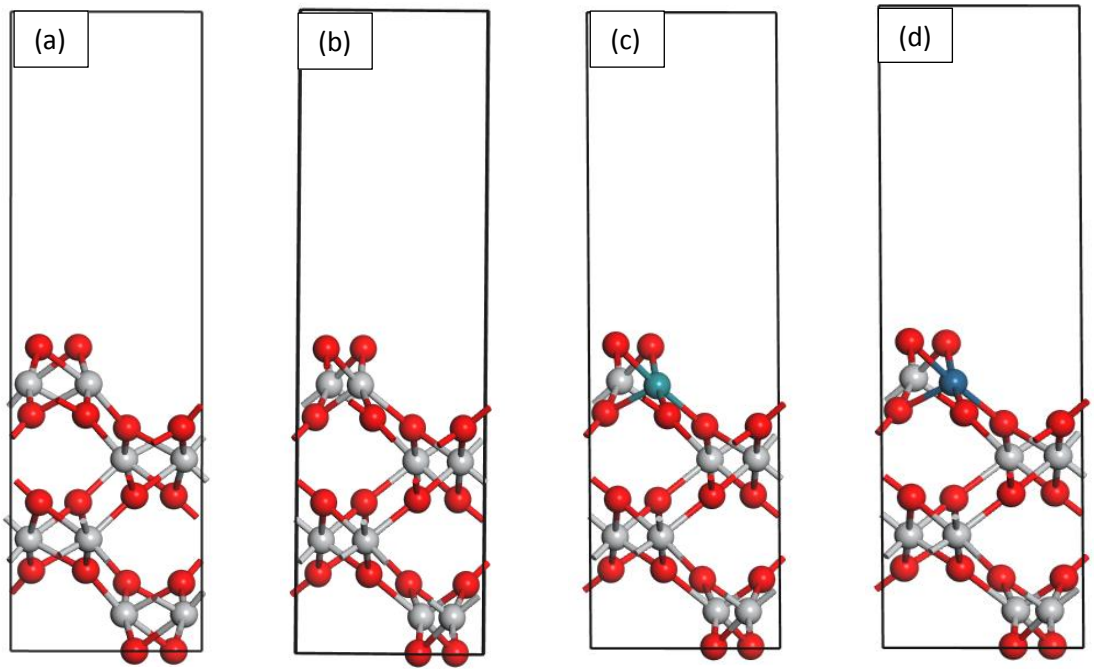

Figure 4. 9 Atomic structures of (a) undoped brookite TiO_2 (100) surface before optimization, (b) undoped brookite TiO_2 (100) surface after optimization, (c) Ru-doped brookite TiO_2 (100) surface after optimization, (d) Pt-doped brookite TiO_2 (100) surface after optimization. The grey spheres, the red spheres, the light blue sphere and blue represent Ti atoms, O atoms, transition metal Ru and Pt respectively.

Figure 4.9 shows the structures of the undoped and doped brookite surfaces before and after optimization, the atomic surface underwent relaxation, but not reconstruction. For all the surfaces, the top and bottom layers of oxygen ions are still 2-fold coordinated (O_{2c}), with the nearest titanium ions being 5-fold coordinated (Ti_{5c}). Table 4.3 illustrates the structural parameters of all four structures after optimization. The results show that the lattice parameters *a* and *b* do not change significantly as compared to the lattice parameter c after doping with Ru and Pt.

Table 4. 2 Optimized structural parameters for surface TiO_2

	Undoped TiO_2	Ru- doped TiO_2	Pt-doped TiO_2
a (Å)	5.558	5.560	5.553
b (Å)	5.300	5.303	5.318
c (Å)	18.556	18.706	18.703

4.3.1.2 (210) Surface

A schematic representation of the brookite (210) surface is depicted in Figure 4.10. The truncation of the octahedral renders different coordination combinations for the outermost titanium cations. The (210) surface is a step surface, which consists of 2-fold coordinated oxygen ions in both the top and the bottom layers. It also has mixture of 2-fold and 3-fold coordinated oxygen ions within the middle layers. The titanium ions are 5-fold and 6-fold coordinated. The atoms in these structures are having some cleaved bonds in the termination position, while terminating with both oxygen and titanium. All the undoped and doped (210) brookite surface structures were optimized by relaxing surface atoms to eliminate surface atomic tension.

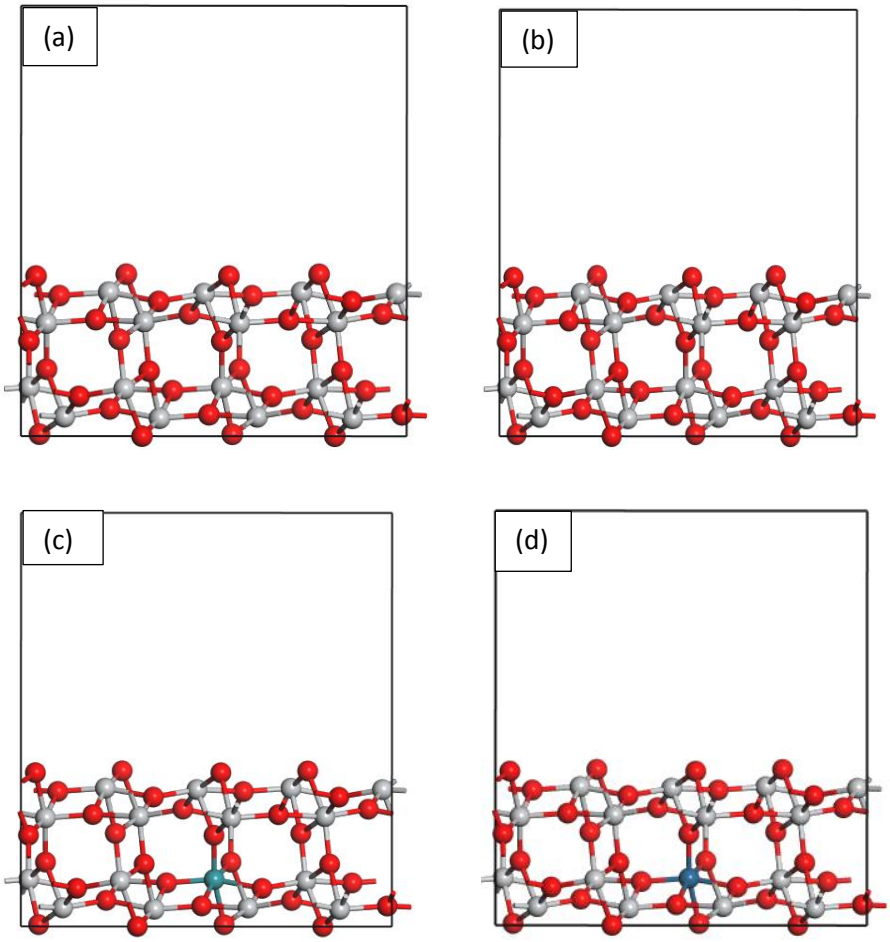

Figure 4. 10 Atomic structures of (a) undoped brookite TiO_2 (210) surface before optimization, (b) undoped brookite TiO_2 (210) surface after optimization, (c) Ru-doped TiO_2 brookite (210) surface after optimization, (d) Pt-doped brookite TiO_2 (210) surface after optimization. The grey spheres, the red spheres, the light blue sphere and blue represent Ti atoms, O atoms, Ru atom and Pt atom respectively.

Relaxation is a small and subtle rearrangement of the surface layers which may nevertheless be significant energetically, and seems to be common place for metal surfaces. It involves adjustments in the layer spacings perpendicular to the surface, there is no change either in the periodicity parallel to the surface or to the symmetry of the surface. Figure 4.10 shows the structures of brookite surfaces before and after optimization. The atomic surface underwent relaxation, but not reconstruction for undoped surface. The doped surface structures undergo small change in the lattice position since the position of the dopant in the case of Pt move downward and for the Ru doped TiO_2 all the atoms to the right of the dopant move upward. Table 4.3 illustrates the structural parameters of all three structures after optimization. It can be

observed that the lattice parameter *a* and *b* of Ru-doped structures do not change much compared to those of undoped structures, while the lattice parameter of Pt-doped surface structure showed a notable change. These findings confirm the fact that after doping there are some reconstructions of the doped surface structures.

Table 4. 3 Optimized structural parameters for surface TiO_2

	Undoped TiO_2	Ru- doped TiO_2	Pt-doped TiO_2
a (Å)	5.317	5.375	5.438
b (Å)	13.870	13.785	13.985
c (Å)	12.294	12.886	12.319

4.3.1.3 (110) surface

All the undoped and doped (110) brookite surface structures were optimized by relaxing surface atoms to eliminate surface atomic tension. The ideal (110) brookite surface is characterized by the presence of pairs of coordinative unsaturated ions, i.e., 5-fold coordinated Ti (Ti_{5c}) and two types of 2-fold coordinated oxygen ions (O_{2c}, O'_{2c}), these atoms having only one cleaved bond. The ideal (110) brookite surface also consists of some 3-fold coordinated O (O_{3c}). The dopants were introduced by replacing one 5-fold Ti element. Table 4.4 below shows the structural parameters of all three structures after optimization. It can be observed that all structures went through relaxation which is a small and subtle rearrangement of atomic positions not reconstruction. This can be observed in Table 4.4, where the lattice parameter *a, b* and *c* for both Pt and Ru doped systems showed a small difference relative to the undoped system.A schematic representation of the brookite (110) surface is depicted in Figure 4.11.

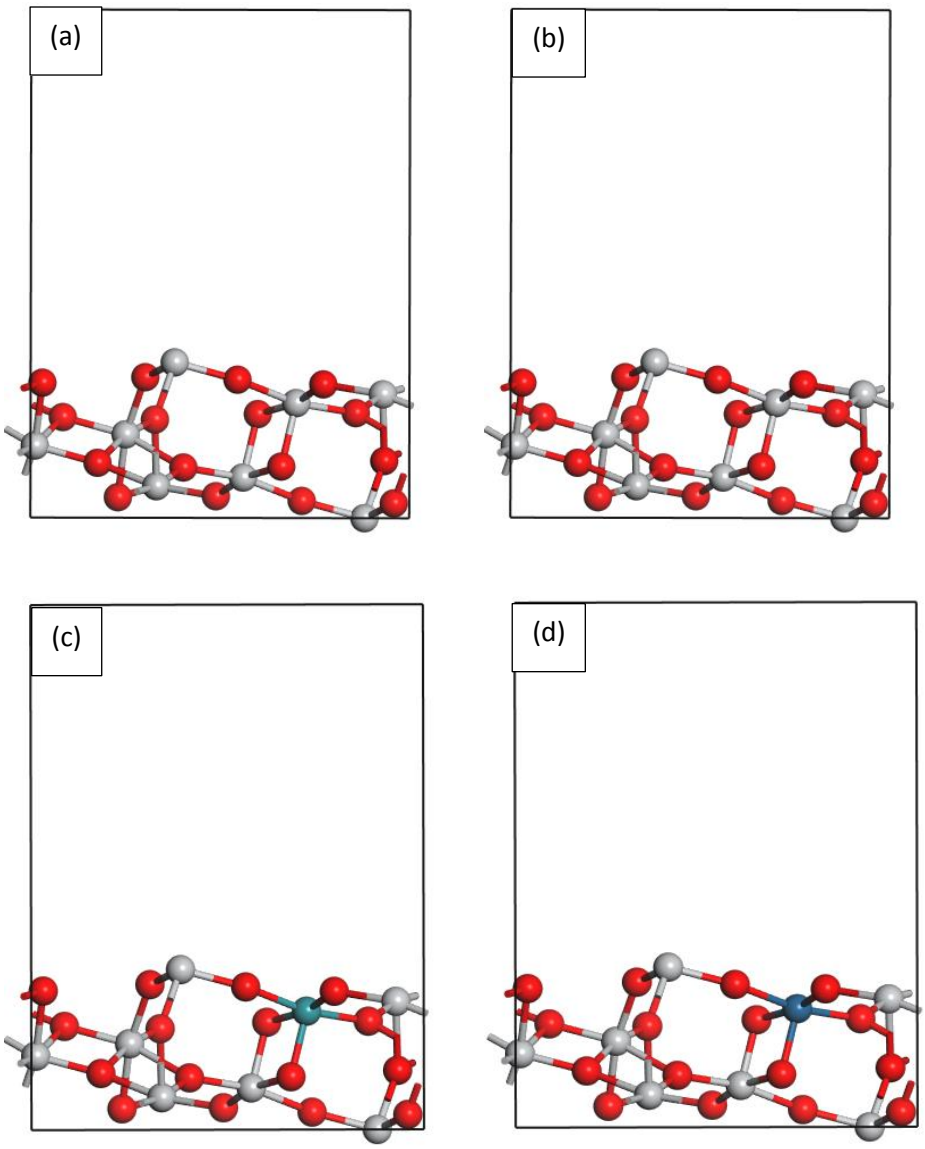

Figure 4. 11 Atomic structures of (a) undoped brookite TiO_2 (110) surface before optimization, (b) undoped brookite TiO_2 (110) surface after optimization, (c) Ru-doped TiO_2 brookite (110) surface after optimization, (d) Pt-doped brookite TiO_2 (110) surface after optimization. The grey spheres, the red spheres, the light blue sphere and blue represent Ti atoms, O atoms, Ru atom and Pt atom respectively.

Table 4. 4 Optimized structural parameters for surface TiO_2

	Undoped TiO_2	Ru- doped TiO_2	Pt-doped TiO_2
a (Å)	5.661	5.775	5.766
b (Å)	11.360	11.385	11.371
c (Å)	14.725	14.672	14.617

4.3.2 Electronic Properties

To conveniently investigate the electronic structures of transition metal-doped brookite TiO_2 surfaces, we set the same k-points mesh to sample the first Brillouin zone for undoped and transition metal doped surfaces.

4.3.2.1 (100) Surface

The calculated band gap of both doped and undoped (100) brookite TiO_2 surfaces was found to be underestimated compared with the experimental value, this is due to the limitations of DFT. However, the discussions on energy band gap are not affected because only the relative energy changes are of concern. In this work, we employed the scissor operation of 1.047 eV to compensate for the underestimation of the band gap. The value of the “scissors” operation used for these surfaces is the same as the one applied on the bulk structure calculations.

The calculated energy band gap of pure brookite TiO_2 (100) surface is 3.35 eV as shown in Figure 4.13. The conduction band minimum is located at G, while the valence band maximum is located near G. Therefore, the brookite TiO_2 (100) surface can be considered as a direct band gap semiconductor. The value of band gap is consistent with the reported literature results [75]. The valence band energy in the pure surface near the Fermi level is from 0 to 4.4 eV and the width is 4.4 eV, which is mainly attributed to the O 2p orbit and Ti 3d orbit hybridization. The conduction band energy is from 2.5 to 20 eV and the width is 17.5 eV, mainly constituted by the Ti 3d track and

a small amount of O 2p track. After doping of transitional metal the band gap narrowed, which is in support of the results reported by Wang et al. [22] who reported that most transition metal doping can narrow the band gap of TiO_2, leading to the improvement in the photo reactivity of TiO_2, and simultaneously maintain strong redox potential.

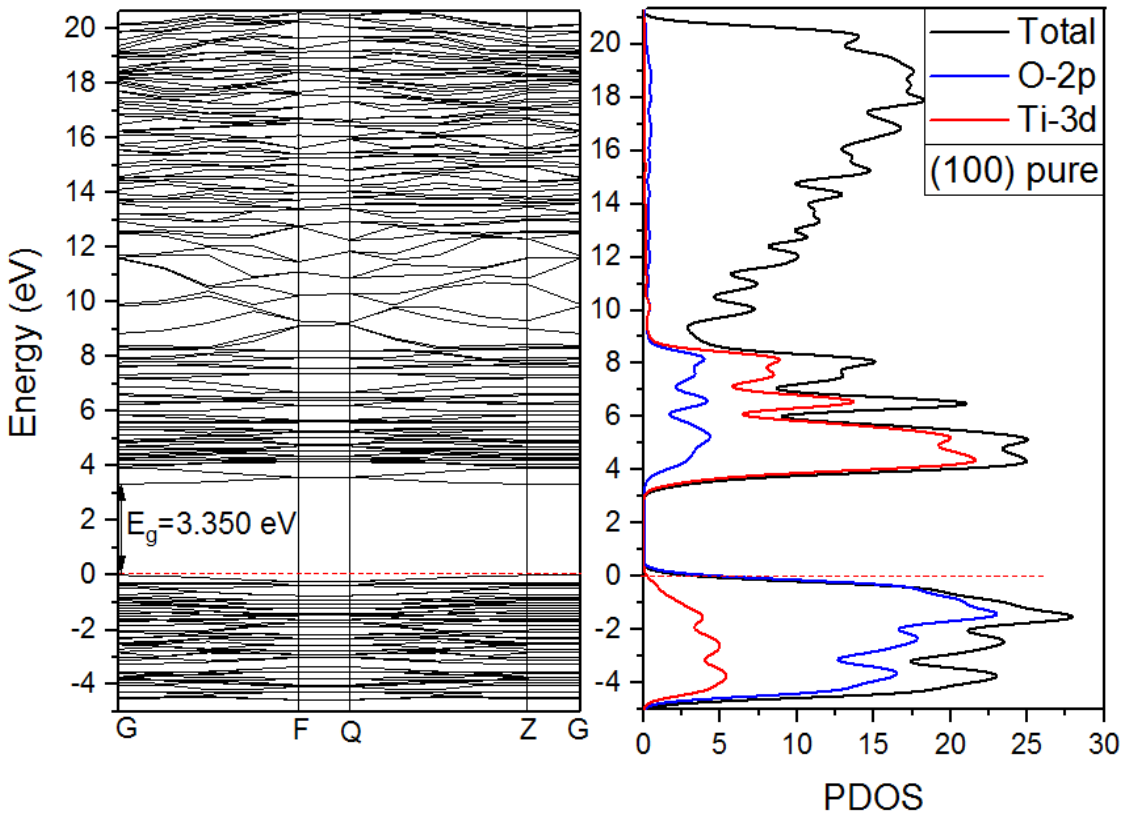

Figure 4. 12 Band structure and density of state of undoped brookite TiO_2 (100) surface.

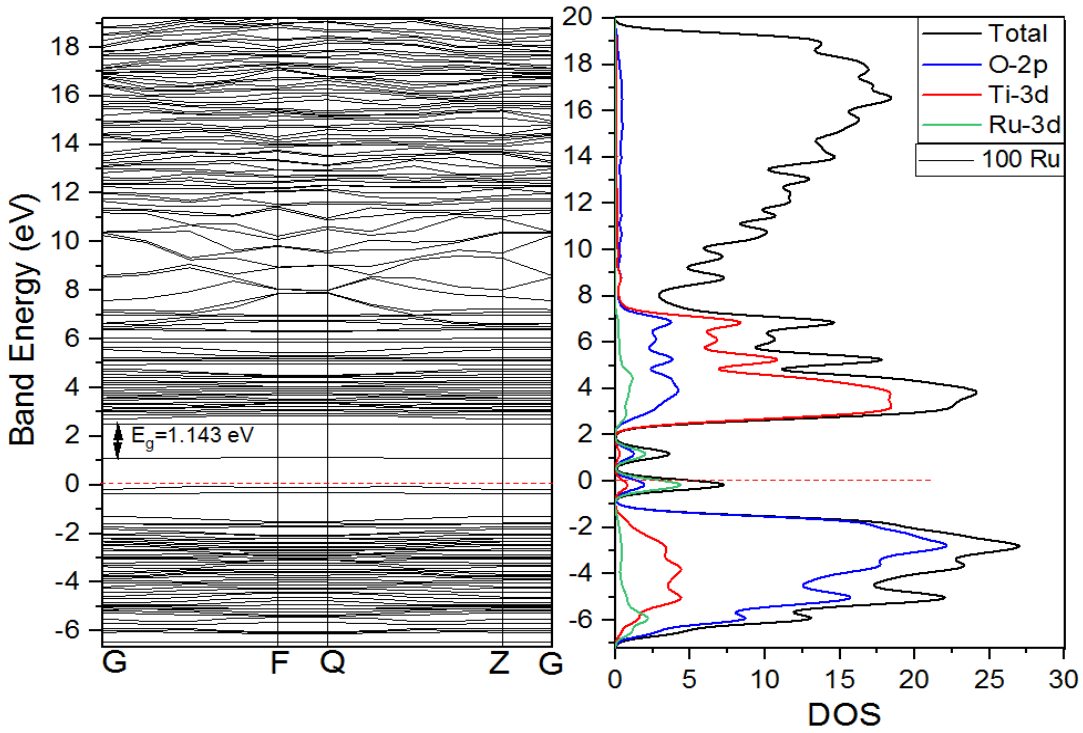

Figure 4. 13 Band structure and density of state of Ru doped brookite TiO_2 (100) surface.

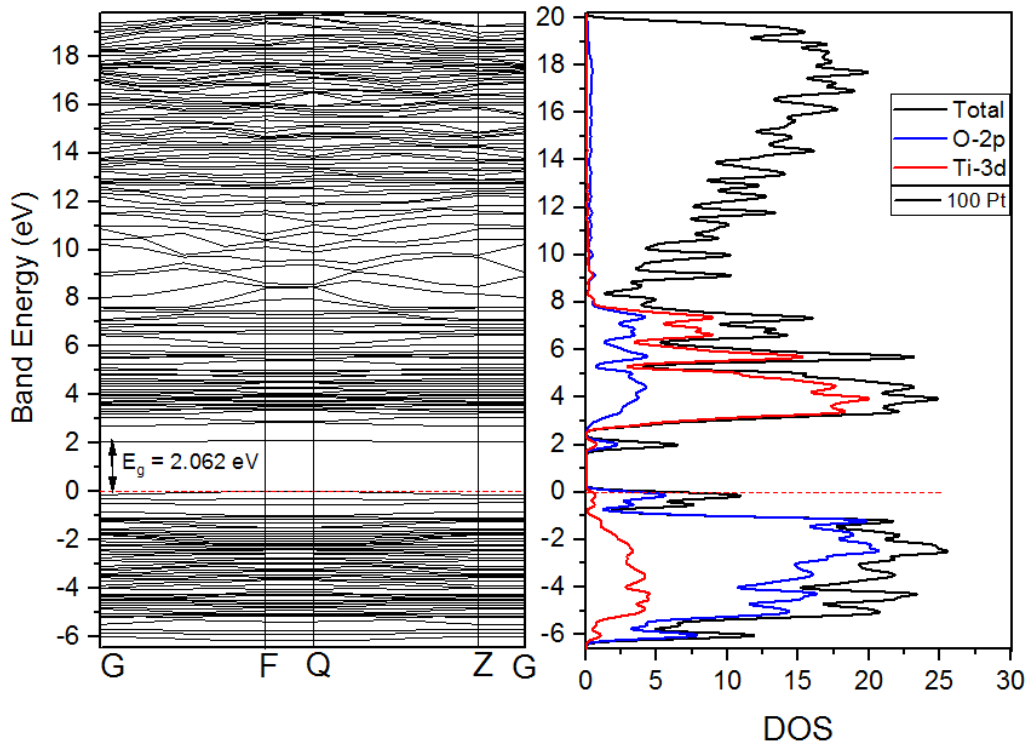

Figure 4. 14 Band structure and density of state of Pt-doped brookite TiO_2 (100) surface.

The total density of states (TDOS) and partial density of states (PDOS) of Ru and Pt -doped brookite TiO_2 (100) surfaces are shown in Figures 4.13 and 4.14 respectively, which were plotted using Originlab. The TDOS shape of transition metaldoped TiO_2 becomes broader than that of pure TiO_2, which indicates that the electronic nonlocality is more obvious, owing to the reduction of crystal symmetry. The transition metal 3d and 5d states are somewhat delocalized, which contributes to the formation of impurity energy levels (IELs) by hybridization with O 2p states or Ti 3d states. Such hybrid effect may form energy levels in the band gap or hybrid with CBM/VBM, providing trapping potential well for electrons and holes. It gives a contribution to separation of photogenerated electron–hole pairs, as well as in favour of the migration of photo excited carriers and the process of photocatalysis. The band gaps of brookite TiO_2 (100) surface doped with Ru and Pt are determined as 1.143 eV, and 2.062 eV, respectively. It is worth noting that the band gap of Ru and Pt –doped TiO_2 surfaces is not related to the band gap between the Ti t_{2g} (d_{xy}, d_{xz}, d_{yz}) and e_g (d_{z^2}, $d_{x^2-y^2}$) bands, but to the energy separation between the O 2p and the Ti t_{2g} bands of TiO_2 that is modified by doping atoms.

4.3.2.2 (210) Surface

The knowledge of the electronic band structure of the TiO_2 polymorphs is useful to understand the photocatalytic behaviour of the pure systems and of their doped counterparts. The highest and lowest energy levels of a band are referred to as the band edges**.** The energy band gap of TiO_2 (210) surface is 4.418 eV; relative to the energy band gap of the bulk system. The band gap is larger than that of the bulk system by 1.018 eV. In the lateral and inner surfaces, the electronic wave function changes in index relations attenuation. The larger band gap for brookite (210) surface indicates that the distribution probability of the electron is biggest in the surface, i.e., the electron is limited near the surface. This kind of electronic state is called the surface state, and the corresponding energy level is called the surface level. Figure 4.16 clearly shows that in this surface, no surface level appears near the Fermi level, indicating that no surface states exist. These changes can be mainly attributed to the redundant electronics of the brookite TiO_2 (210) surface transfer to the other atoms. The conduction band energy is from 2.5 to 20 eV and the width is 17.5 eV, mainly constituted by the Ti 3d track and a small amount of O 2p track. For the undoped

surface the valence band energy near the Fermi level is from 0 to 4.0 eV and the width is 4.0 eV, which is also attributed to the O 2p orbit and Ti 3d orbit hybridization. The conduction band energy is from 4.2 to 20 eV and the width is 15.8 eV, mainly constituted by the Ti 3d track and a small amount of O 2p track. The width of the conduction band for an undoped surface is smaller and the electrons are locally enhanced near surfaces. Compared with the band of the bulk system, the brookite TiO_2 (210) surface band is smoother, and the corresponding surface state density peak is higher than that of the bulk phase. This result can be attributed to two reasons: first, the system is made up of different numbers of atoms; second, the band gap width changes strengthening the surface electronic density of states and localization.

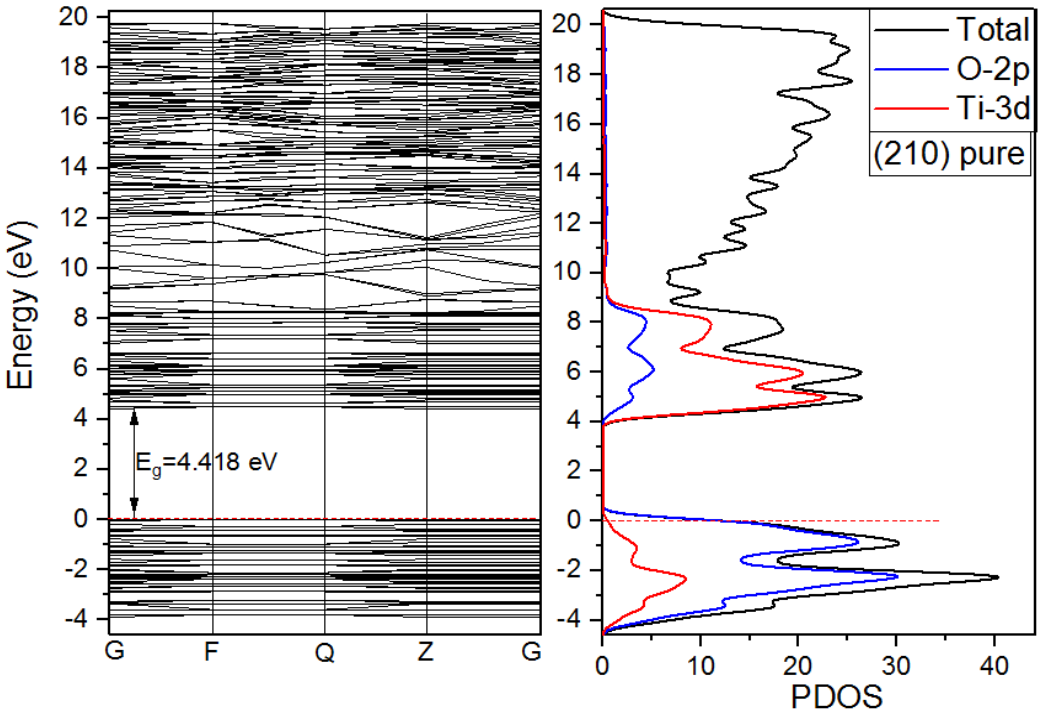

Figure 4. 15 Band structure and density of state of undoped brookite TiO_2 (210) surface.

In the case of Ru or Pt doped brookite TiO_2 (210) surfaces, considering the underestimation of the calculations, the band gaps of the Ru and Pt doped brookite TiO_2 are corrected by scissors operator. The scissors operator is set at 1.047 eV, accounting for the difference between the experimental band gap (3.23 eV) and the calculated band gap (2.21 eV) for bulk brookite TiO_2. Then, the band gap Ru and Pt doped TiO_2, are determined as 1. 335 eV shown in Figure 4.17 and 2.296 eV shown in Figure 4.18. Lower band gap value of the doped systems in comparison with the

undoped (210) is evident that doping with transitional metal results in the narrowing of the band. The band gap is narrowed by the formation of the impurity energy levels, which are a result of hybridizing with O 2p states or Ti 3d states. It gives a contribution to separation of photo generated electron–hole pairs, as well as in favour of the migration of photo excited carriers and the process of photocatalysis. The impurity energy levels are located above the VB and partially overlap with the VBM in both Pt-TiO_2 and Ru-TiO_2 (210) surfaces. These kinds of IELs could act as trap centres for photoexcited holes, which can also reduce the recombination rate of charge carriers.

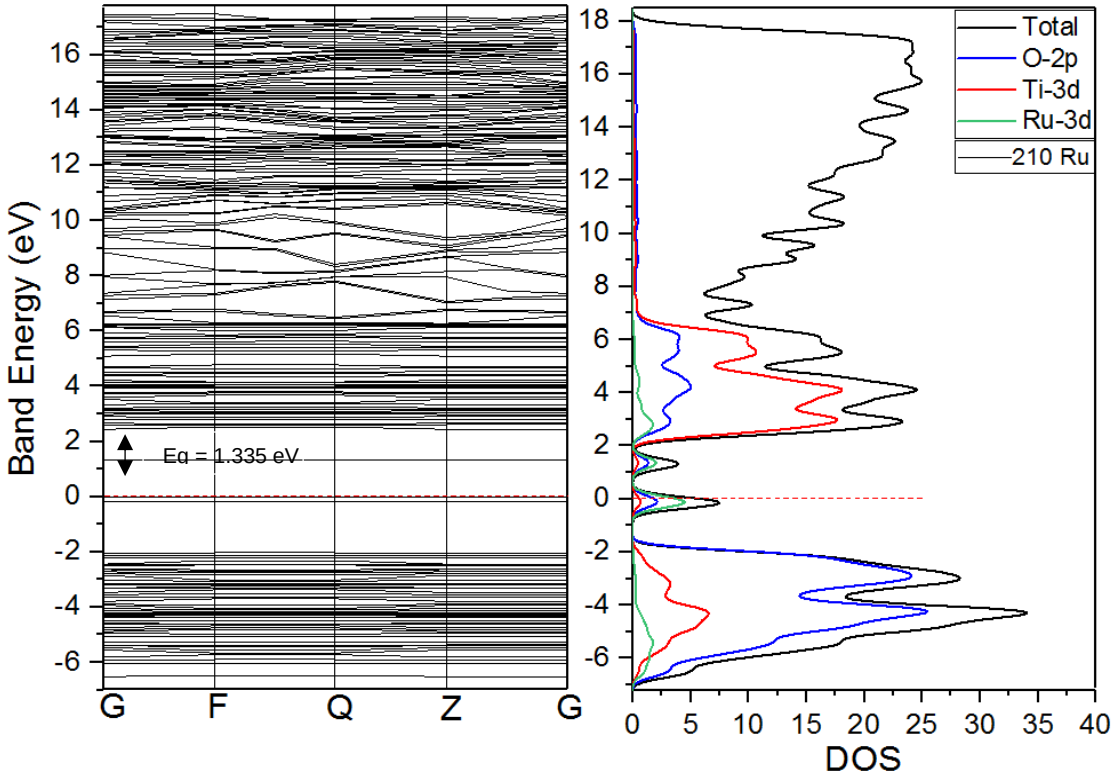

Figure 4. 16 Band structure and density of state of Ru-doped brookite TiO_2 (210) surface.

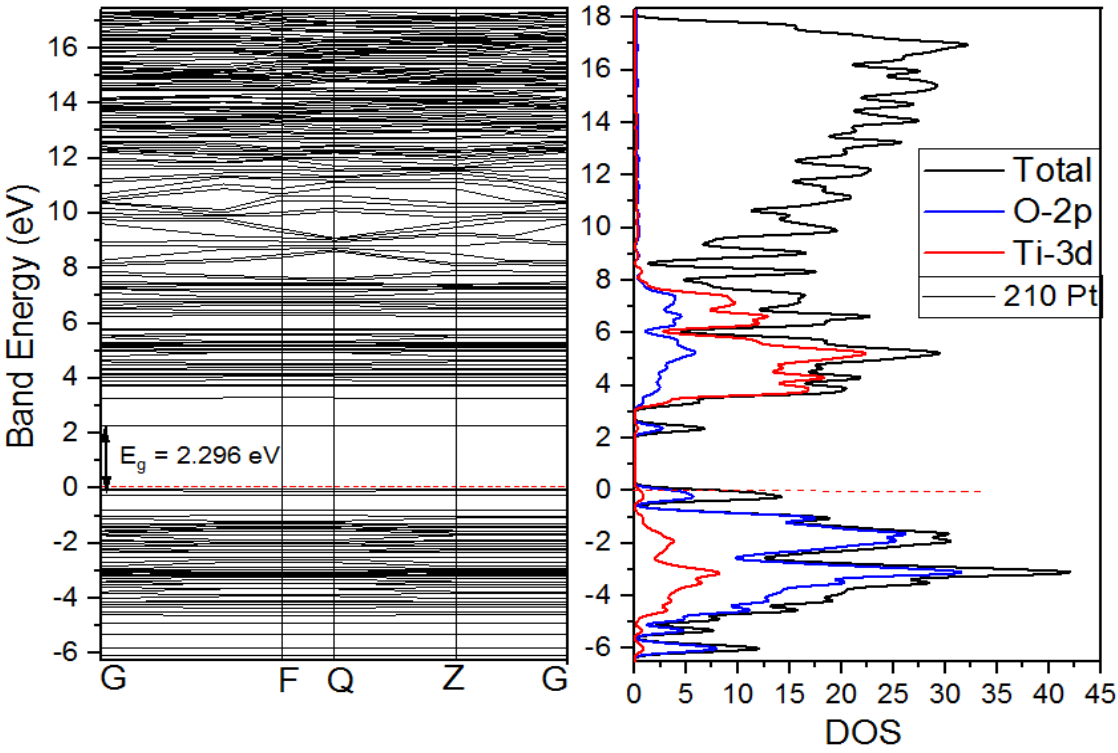

Figure 4. 17 Band structure and density of state of Pt-doped brookite TiO_2 (210) surface.

4.3.2.3 (110) Surface

Figure 4.19 shows the band structure of pure (110) brookite TiO_2 surface. It is observed that the band gap is about 4.572 eV, which in relative to the bulk band gap is larger by 1.172 eV. The results suggest that the distribution probability of the electron is biggest in the surface, i.e., the electron is limited near the surface. This kind of electronic state is called the surface state, and the corresponding energy level is called the surface level. Similar trend was observed for (100) and (210) brookite TiO_2 surfaces. Figure 4.19 shows that in the surface, no surface level appears near the Fermi level, indicating that no surface states exist. These changes can be mainly attributed to the redundant electronics of the brookite TiO_2 surface transfer to the other atoms. The results show that the valence band (VB) of the undoped TiO_2 is mainly composed of the hybridization of O 2p and Ti 3d states while the conduction band (CB) mainly consists of Ti 3d states which demonstrate its consistency with the experimental results [76]. It is clear from the band gap results that the valence band maximum and the conduction minimum occur at approximately same value of G, which proves the fact that the band gap of brookite is direct.

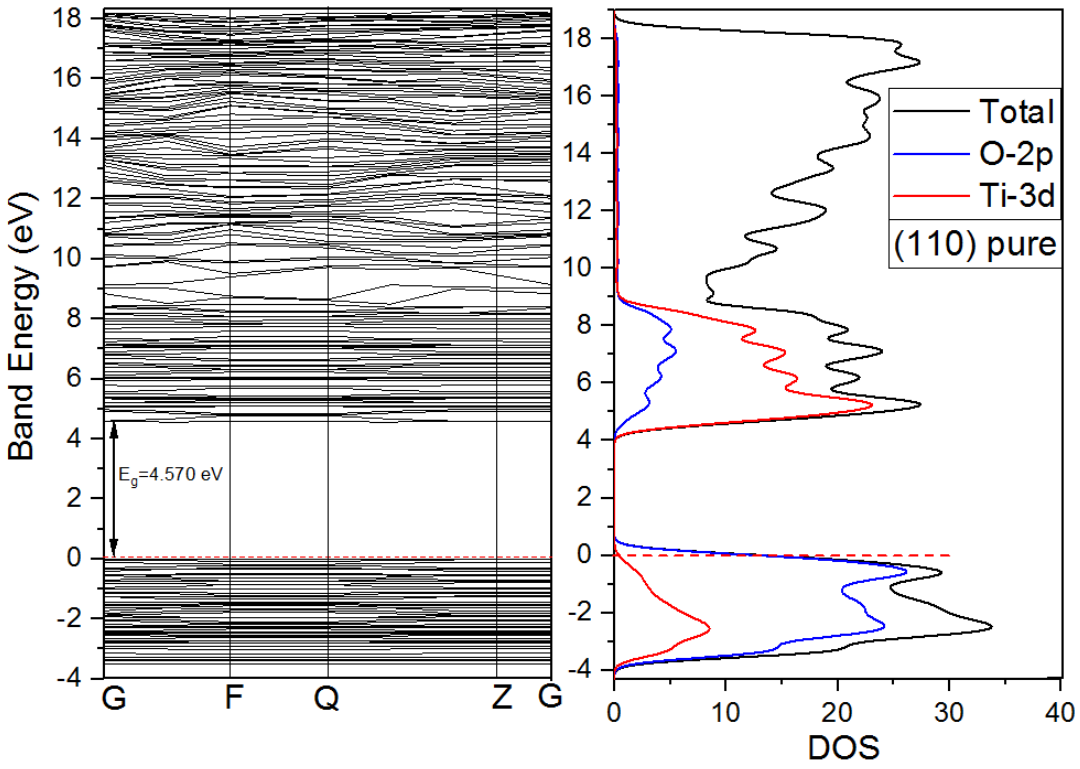

Figure 4. 18 Band structure and density of state of undoped brookite TiO_2 (110) surface.

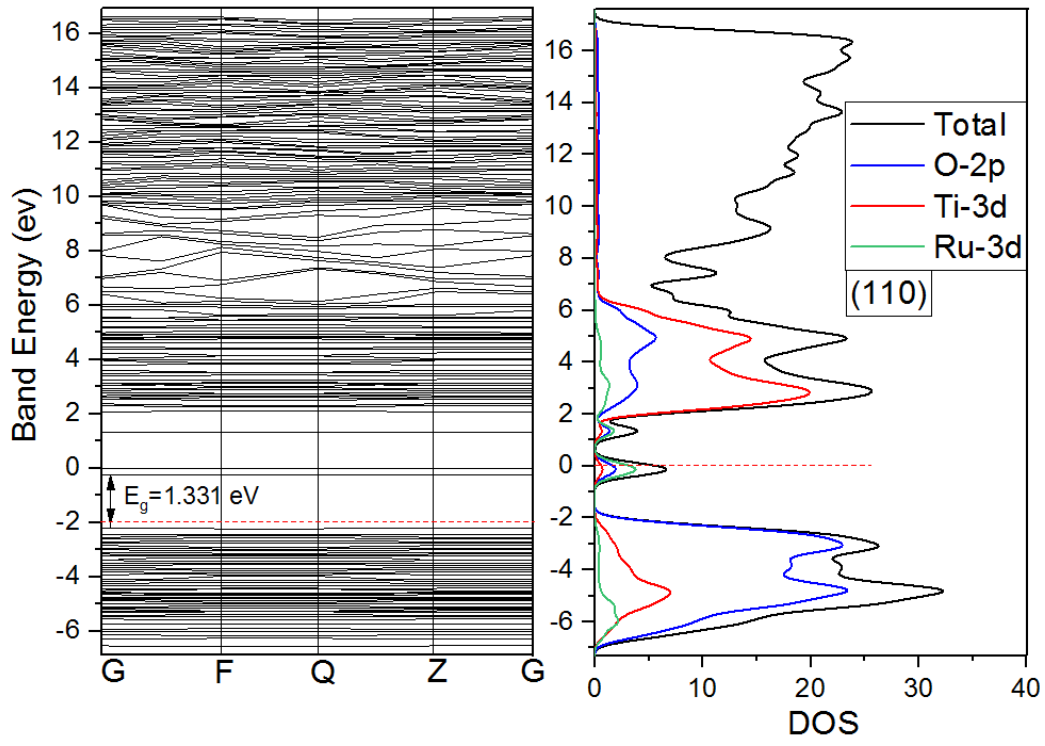

Figure 4. 19 Band structure and state density of Ru-doped brookite TiO_2 (110) surface.

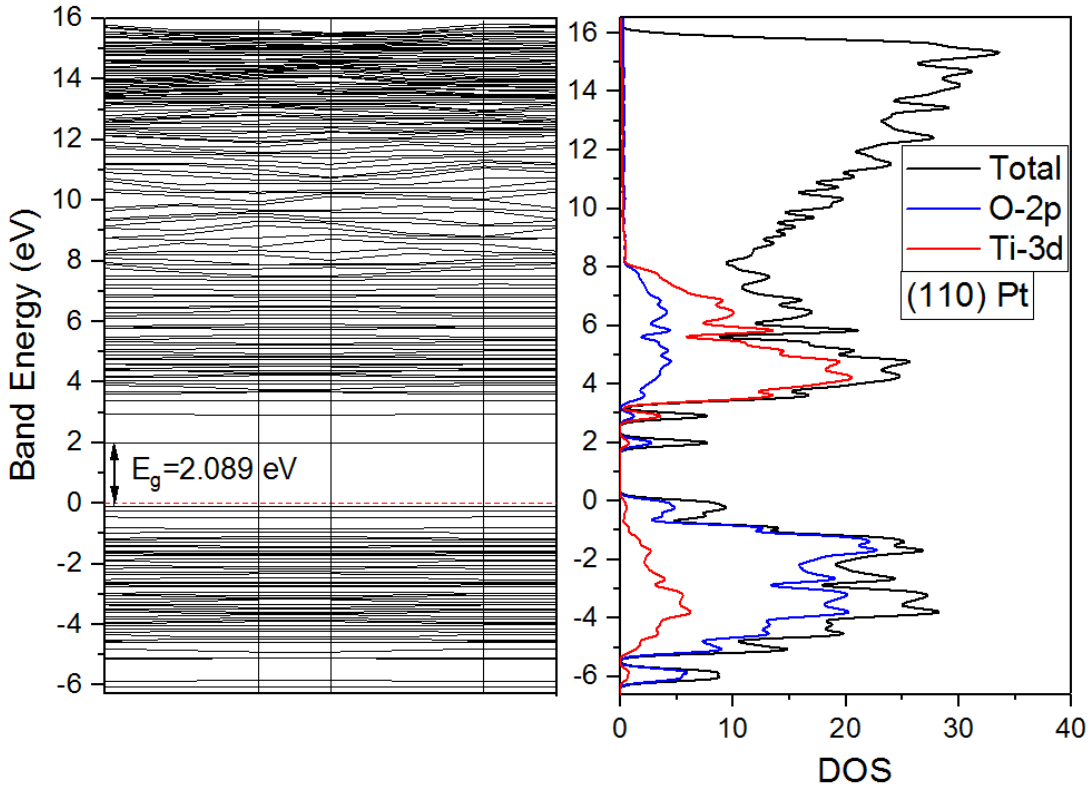

Figure 4. 20 Band structure and density of state of Pt-doped brookite TiO_2 (110) surface.

The DOS for Pt-TiO_2 (110) presented in Figure 4.21 indicates that single Pt at the hollow site interacts with Ti 5c that appears as a Pt–Ti 5c hybridization peak at the bottom of the CB. The non-bonding excess charge around Pt brings four occupied flat gap states above the VBM. For Ru-doped TiO_2, the PDOS calculation corresponding to Ru 3d shows new impurity energy levels sitting above the top of VB. PDOS reveal that Ru 3d states appear as seven isolated impurity energy levels located below the bottom of the conduction band with one of them completely occupied and the others unoccupied. These impurity energy levels sufficiently overlap with conduction band minimum of TiO_2 surfaces. Figures 4.20 and 4.21 show the calculated partial density of states for doped systems. The VB of undoped TiO_2 (110) surface is located between ~ –0.85 and –2.5 eV, mainly formed by O 2s states, which are the intershell electrons. The peak's shape is sharp and the locality is strong for an undoped surface as shown in Figure 19. The width of VB is between ~ –4.0 and 0 eV near the Fermi energy level is ~4.0 eV, and the width of CB is ~ 5.0 eV. The VB and CB are formed mainly by the O 2p states and Ti 3d states, and the former is dominated by O 2p states and the latter

by Ti 3d states. The O 2p and Ti 3d states show resonance phenomenon. This indicates that some covalence bond character between Ti and O atoms exist [51].

It is clear that the CB of Ru-doped TiO_2 is composed mainly of Ti 3d states while the VB is composed mainly of O 2p states. The impurity energy levels located above the top of VB are formed by hybridization of O 2p states and Ti 3d states with Ru 3d states. When the impurity energy levels are taken into account, the CBM is located at ~-0.2 eV since there are some small impurities formed just below the CB, the width of VB is ~-5.6 eV. These kinds of impurity energy levels could act as acceptor levels, which can reduce the recombination rate of charge carriers and thus improve the photocatalytic activity. In the case Pt doped surface, the Pt 5d states are somewhat delocalized. The VB is formed mainly by the O 2p states, and the impurity energy levels located above the top of VB are formed by hybridization of O 2p states and Ti 3d states with 5 d9 6 s1 states. If the impurity energy levels are taken into account, the CBM is located at ~-2.0 eV, the width of CB is ~3.9 eV, and the width of VB is ~-6.2 eV. Compared with undoped surface, the band gap of Pt-doped TiO_2 narrowed to 2.202 eV, due to the mixing of Pt 5 d9 6 s1 states with O 2p states and Ti 3d broadening the width of VB.

4.3.3 Surfaces Optical Properties

4.3.3.1 (100) Surface

The polarized model of TiO_2 was used to calculate the absorption spectra of the various surface systems. The optical calculations were based on the ground state of the electrons. The calculated absorption spectra for undoped, Ru doped, and Pt doped TiO_2 (100) surfaces are shown in Figure 4.22. The Figure 4.22 reveals that the absorption edge of doped TiO_2 surfaces shifts to visible light region with respect to undoped TiO_2 surface. Ru doped surface has the greatest red shift extent. As shown in Figure 4.22 Ru-doped surface has a high peak absorbing from 400 nm towards the infrared (IR) region. The red shift could be caused by impurity energy levels.

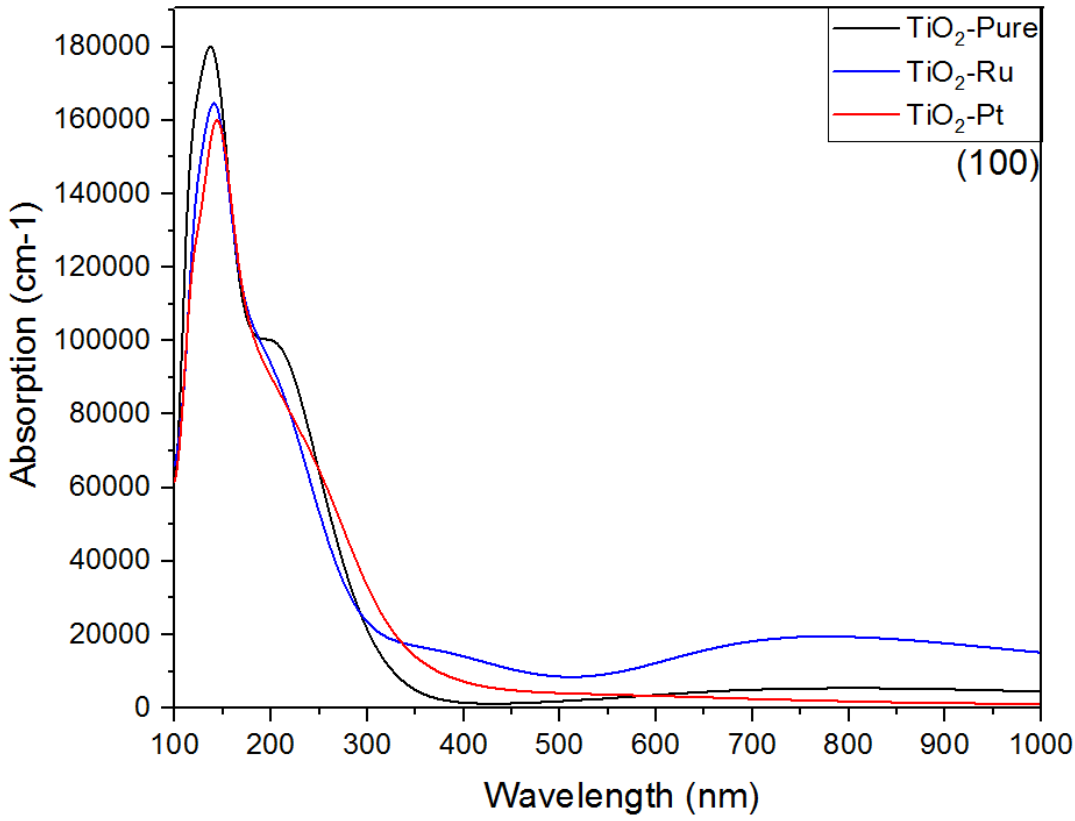

Figure 4. 21 Optical absorption curves of the undoped and doped brookite TiO_2 (100) surface.

The real and virtual parts of the dielectric function versus photon energy change curve are shown in Figure 4.23 and 4.24, respectively. For undoped surface and Ru-doped surface, there are four peak positions in the imaginary part. The first high and sharp peak for both the undoped and Ru doped appears at ~2 eV. This is attributed by the fact that the valence band O 2p states jump to the conduction band Ti 3d states. In addition, there are contributions from Ru 3d states, according to analysis of the energy band diagram and density of states. The second, third and fourth peaks are at ~4 eV, ~11 eV and ~36 eV respectively; mainly owing to the electron transition from the O 2s state to the Ti 3d state. There are no results in literature to compare with. Both the real and imaginary parts of the dielectric function for Pt doped system have number of peaks. The peak for the real part due to the valence band O 2p states jumps to the conduction band Ti3d states and some contribution from Pt 3d state. This peak is at the lower energy than that of undoped and Ru-doped systems.

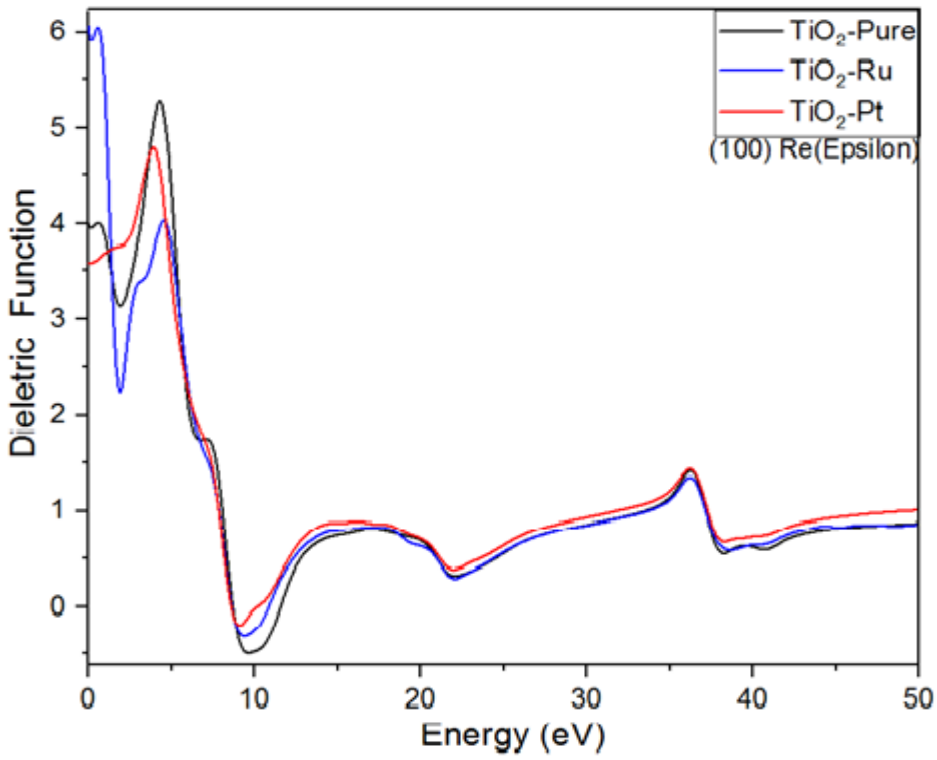

Figure 4. 22 Real part of dielectric function of the undoped and doped brookite TiO_2 (100) surface.

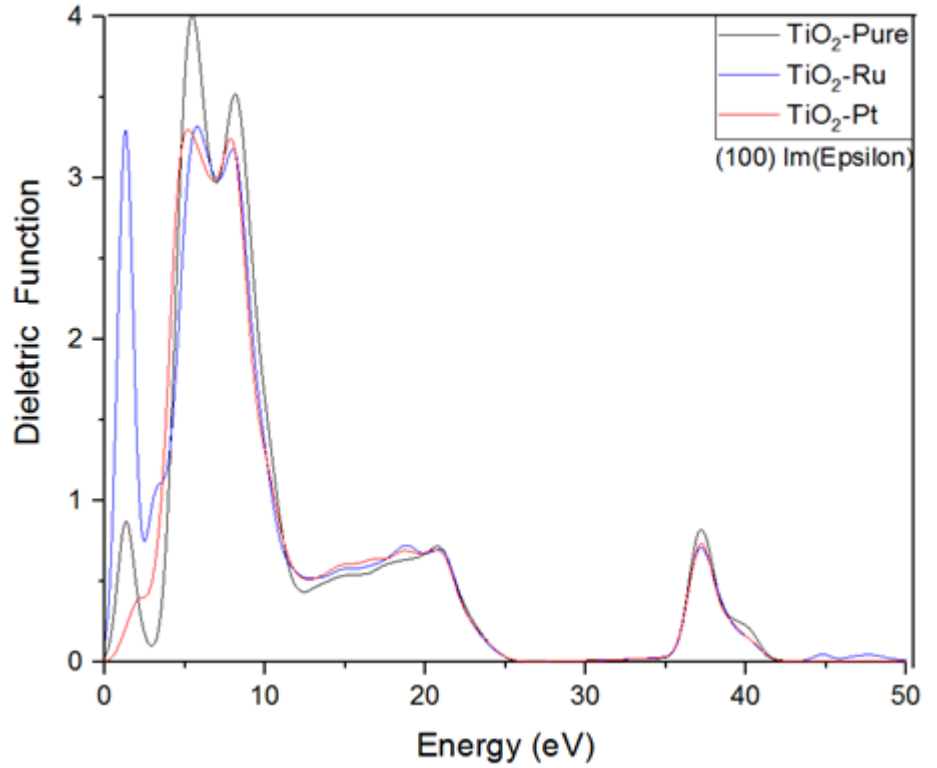

Figure 4. 23 Imaginary part of dielectric function of the undoped and doped brookite TiO_2 (100) surface.

The reflectivity is the ratio of a wave reflected from a surface of energy possessed by the wave striking the surface. The reflectivity spectra for undoped and doped surfaces are displayed in Figure 4.25 as a function of energy. The reflectivity is much higher in the infrared region. The undoped and doped surfaces are showing similar reflectivity spectra patterns, where the first peak is at low energy ranging between 0 and 11 eV, with a splitting at the top. The other two peaks are at ~20 eV and ~38 eV, with decreasing intensity. For Ru-doped the reflectivity spectra is showing four peaks, where three are in the same energy region as those of undoped and Pt doped, but with intensity or low photo energy in some regions. The other peak that only appears in Ru doped is in between 44 eV and 50 eV with a well define shape and low intensity. The large reflectivity for E < 1 eV indicates the characteristics of high conductance in the low energy region. The main energy loss for all the surfaces is at about ~11 eV and ~23 eV. Figures 4.25 and 4.26 reveal that the energy loss peaks for all surfaces correspond to the sharp decline in the reflectivity spectrum.

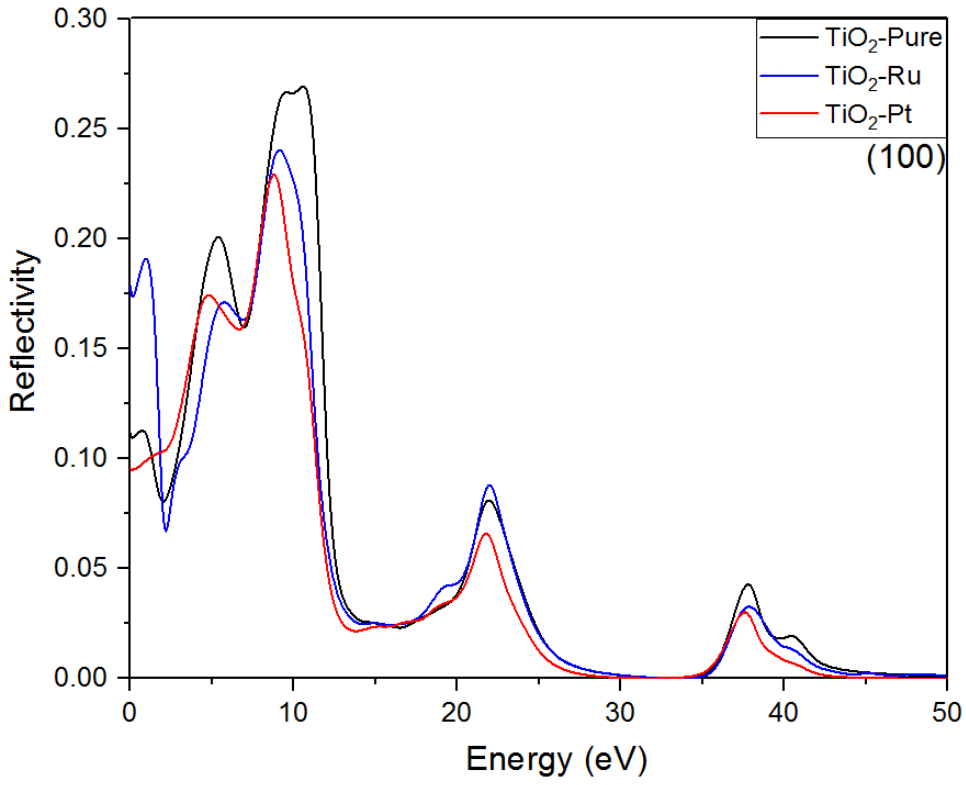

Figure 4. 24 Reflection spectrum of the undoped and doped brookite TiO_2 (100) surface.

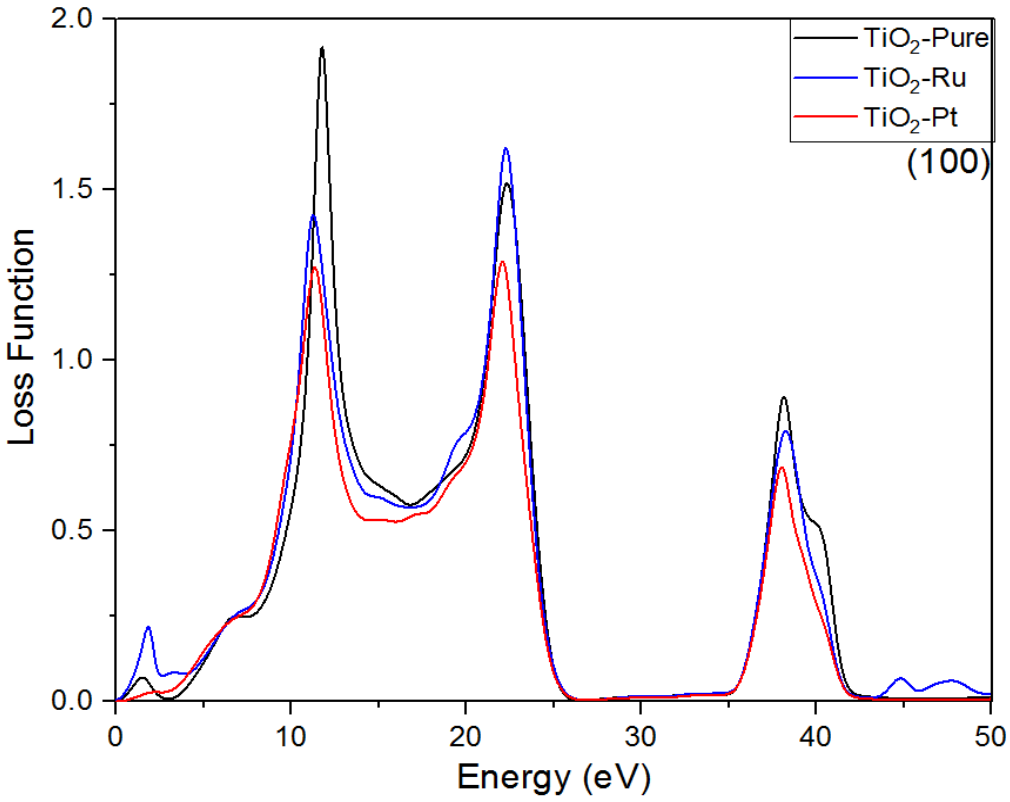

Figure 4. 25 Energy loss function of the undoped and doped brookite TiO_2 (100) surface.

4.3.3.2 (210) Surface

In order to explore the absorption properties, the optical absorption spectra of undoped and Ru or Pt doped (210) surfaces were calculated on the basis of the detailed electronic band structure as discussed in section 4.2. Because of the underestimated band gap of pure TiO_2, we introduced a scissors operator of 1.047 eV (band gap difference between experimental and calculated value) for obtaining some exact optical absorption spectra in the visible region.

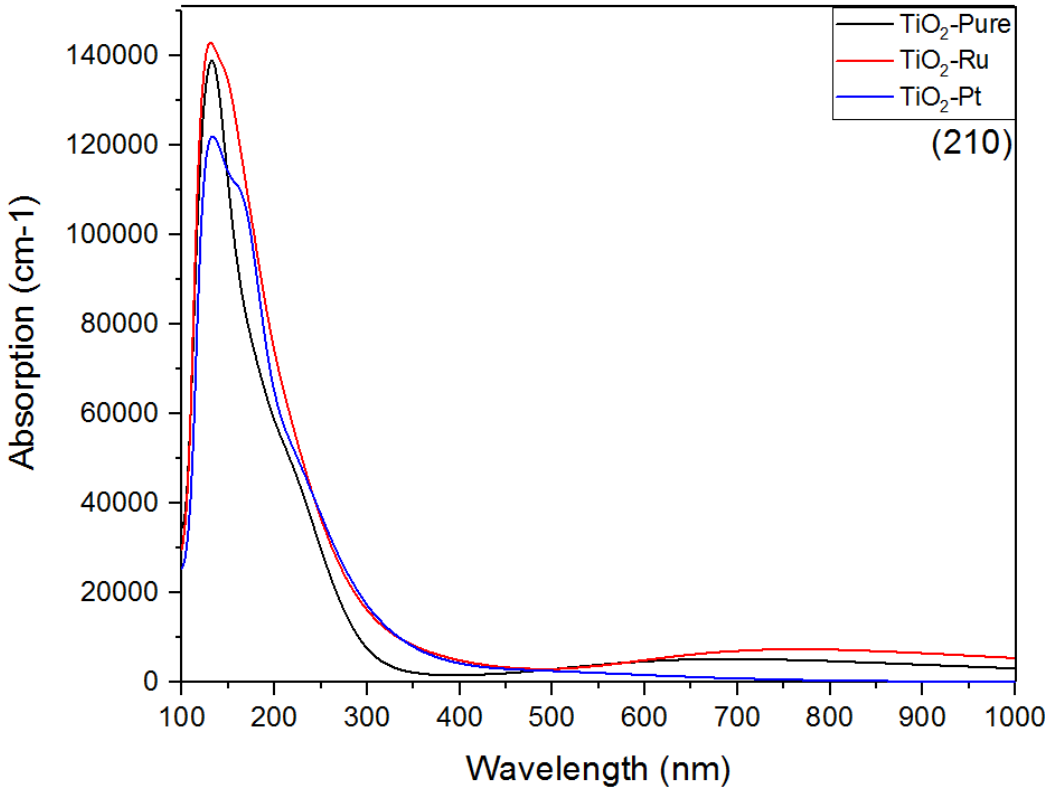

Figure 4. 26 Optical absorption curves of the undoped and doped brookite TiO_2 (210) surface.

The absorption coefficient gives important information about solar energy conversion efficiency and how far light of specific frequency can penetrate into the material before being absorbed. Figure 4.27 reveals that the absorption edges of Ru doped and Pt doped surfaces, move toward the longer wavelength; implying the enhancement of visible light absorption. Pt has stronger light absorption in the visible region as compared to an undoped surface and is the same as that of Ru doped surface. Thus, Pt and Ru doped surfaces have a higher photocatalytic activity. The undoped surface was found to have an absorption in the near infrared region than the Pt doped surface. The impurity band can act as a "step" that reduces the electronic transition energy. Thus, the more electrons can be excited. When more electrons are excited, the greater the probability that photo-excited electrons can migrate into the surface. Meanwhile, the impurity energy levels or band could also act as a separating centre. The photo-excited electrons-holes can separate rapidly and effectively, which will promote the carriers diffusion and enhance the charge carrier lifetime.

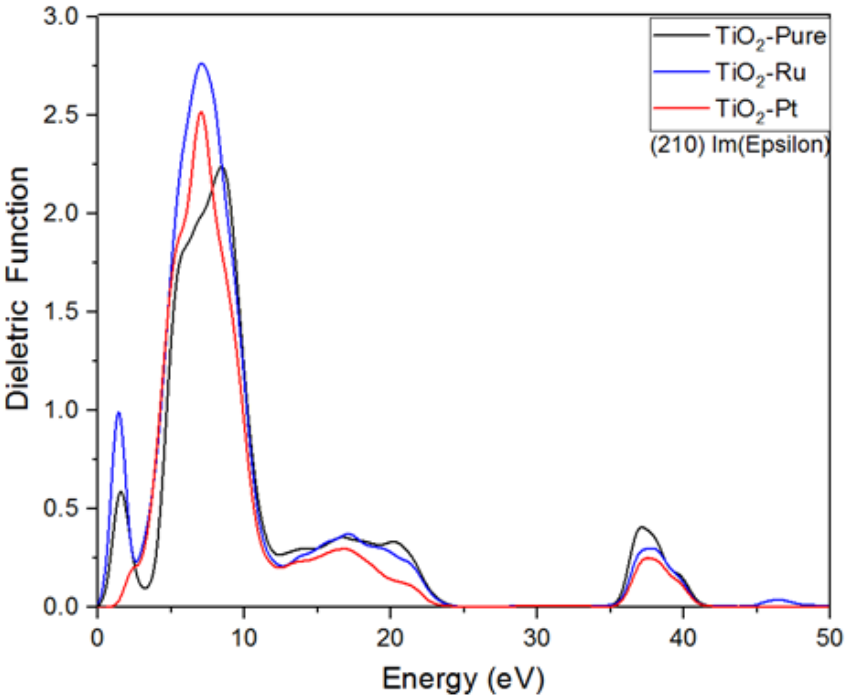

Figure 4. 27 Imaginary part of dielectric function of the undoped and doped brookite TiO_2 (210) surface.

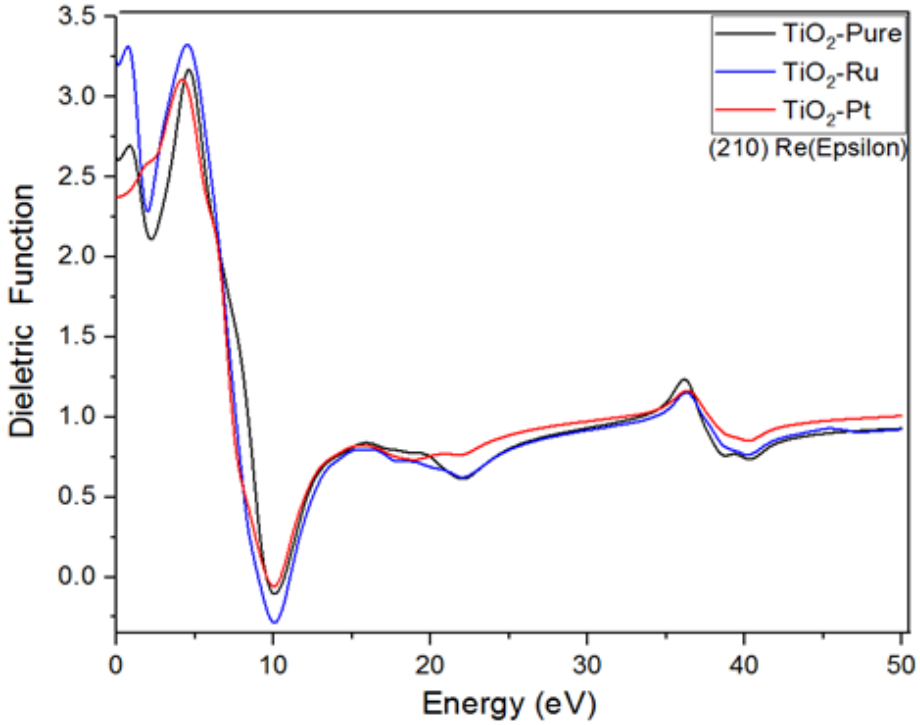

Figure 4. 28 Real part of dielectric function of the undoped and doped brookite TiO_2 (210) surface.

The dielectric function describes the polarization and absorption of the material. The real and imaginary parts of the dielectric function versus photon energy change curve are shown in Figure 4.28 and 4.29 respectively. It can be observed that the value of imaginary part of the dielectric function is zero between ~24 and 35 eV for all the surfaces. Therefore, these materials become transparent in this region and above 50 eV. Also, the real part of dielectric function falls below zero at about 10 eV for all the surfaces. This corresponds to the energy at which the reflectivity exhibits a sharp drop and the energy loss function shows a prominent peak. The peak of the imaginary part of the dielectric function is related to the electron excitation. For the imaginary part of all the surfaces, the peak for E <1 eV is due to intraband transitions and this peak for Pt doped was found to be at lower energy as compared to those of undoped and Ru doped surfaces.

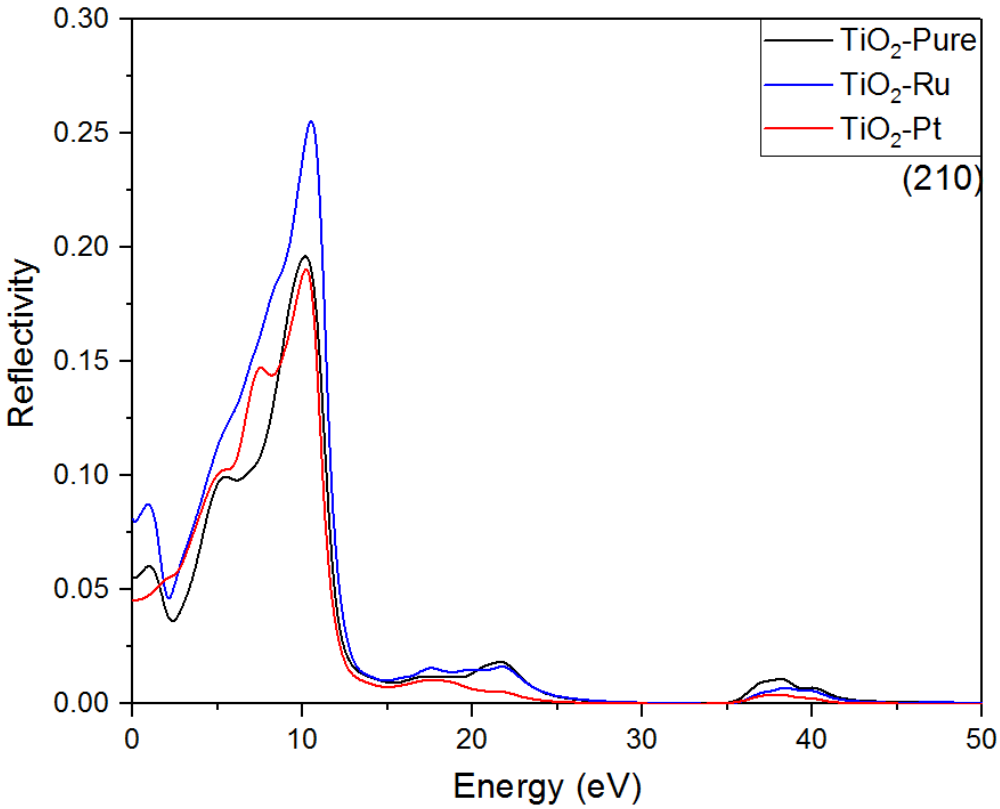

Figure 4. 29 Reflection spectrum of the undoped and doped brookite TiO_2 (210) surface.

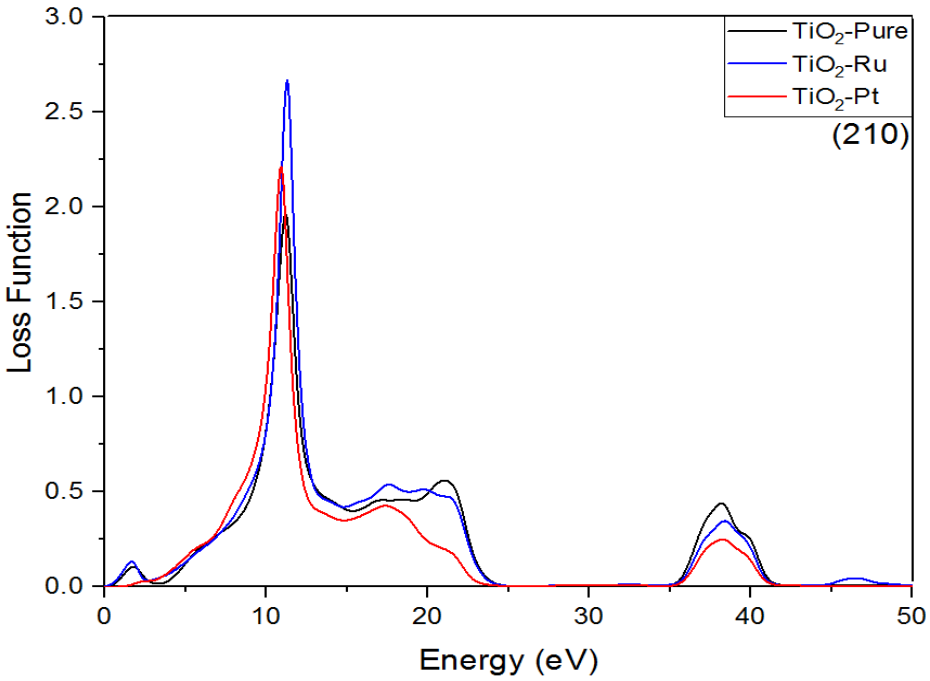

Figure 4. 30 Energy loss function of the undoped and doped brookite TiO_2 (210) surface.

The reflectivity spectra of undoped and doped surfaces are displayed in Figure 4.30 as a function of energy. Similar to (100) surface, reflectivity is much higher in the infrared region. The undoped and doped surfaces are showing similar reflectivity spectra patterns, where the first peak is at low energy ranging between 0 and 13 eV, with a splitting at the top. The other two peaks are at ~23 eV and ~39 eV, with decreasing intensity. The reflectivity spectrum for Pt doped surface is composed of four peaks, where three are in the same energy region as those of undoped and Ru doped surfaces. The large reflectivity for E < 1 eV indicates the characteristics of high conductance in the low energy region. The energy loss function of a material is a parameter that describes the energy loss of a fast electron traversing that material. The frequency associated with the highest peak of energy loss spectrum is defined as the bulk plasma frequency ω_p of the material, which appears at $\epsilon_2 < 1$ and $\varepsilon_1 = 0$ [77].

The energy loss spectra of all surfaces are depicted in Figures 4.31 as a function of photon energy. For all surfaces, there are two major peaks found at 11.50 eV and 39 eV, which indicate the rapid reduction in the reflectance. The Pt doped surface shows an extra peak on the shoulder of the 11.50 eV, which is not present on other surfaces. When the incident photon energy is higher than 40 eV, all surfaces will become transparent.

4.3.3.3 (110) Surface

On the basis of the electronic band structure, the optical absorption spectra of undoped and doped TiO_2 surfaces between 100 nm and 1000 nm are shown in Figure 4.32. It can be observed that the absorption edge of all the doped TiO_2 shifts to visible light region with respect to pure TiO_2, and Ru doped TiO_2 has a greatest red shift extent, with the undoped surface showing absorption only on UV region, which is the low wavelength region. The Ru doped surface show the highest absorption in the range between 380 nm and 1000 nm, the Pt doped shows absorption in the visible region and a small part of the infrared region. As all the doped TiO_2 surface have a lower band gap than pure TiO_2 surface, the red shift could possibly be caused by impurity energy levels.

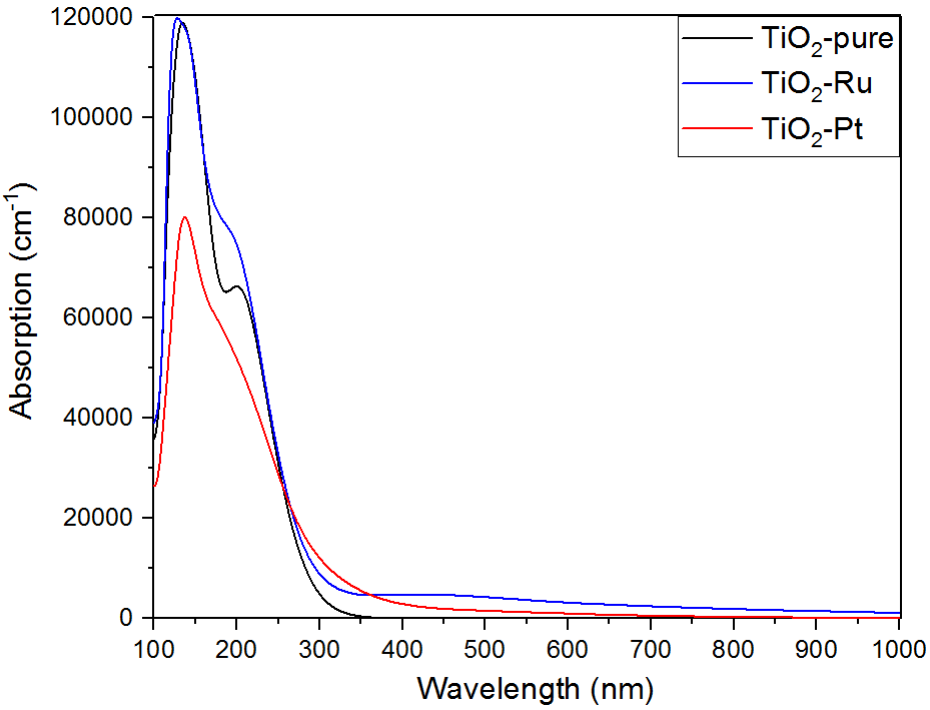

Figure 4. 31 Optical absorption curves of the undoped and doped brookite TiO_2 (110) surface.

The real and virtual parts of the dielectric function versus photon energy change curves are shown in Figure 4.32 and 4.33 respectively. It is observed that the value of imaginary part of the dielectric function is zero between 24 eV and 35 eV for all surfaces, hence these materials become transparent at this region and above 44 eV, but Ru doped shows another small peak between 45 eV and 50 eV. We also observe that the real part of dielectric functions real part falls below 0 at about 10 eV for Ru

doped surfaces. These correspond to the energy at which the reflectivity exhibits a sharp drop and the energy loss function shows a prominent peak. The peak of the imaginary part of the dielectric function is related to the electron excitation. For the imaginary part of all surfaces, the peak for E < 1eV is due to intraband transitions and this peak for Pt doped was found to be at lower energy as compared to the un doped and Ru doped.

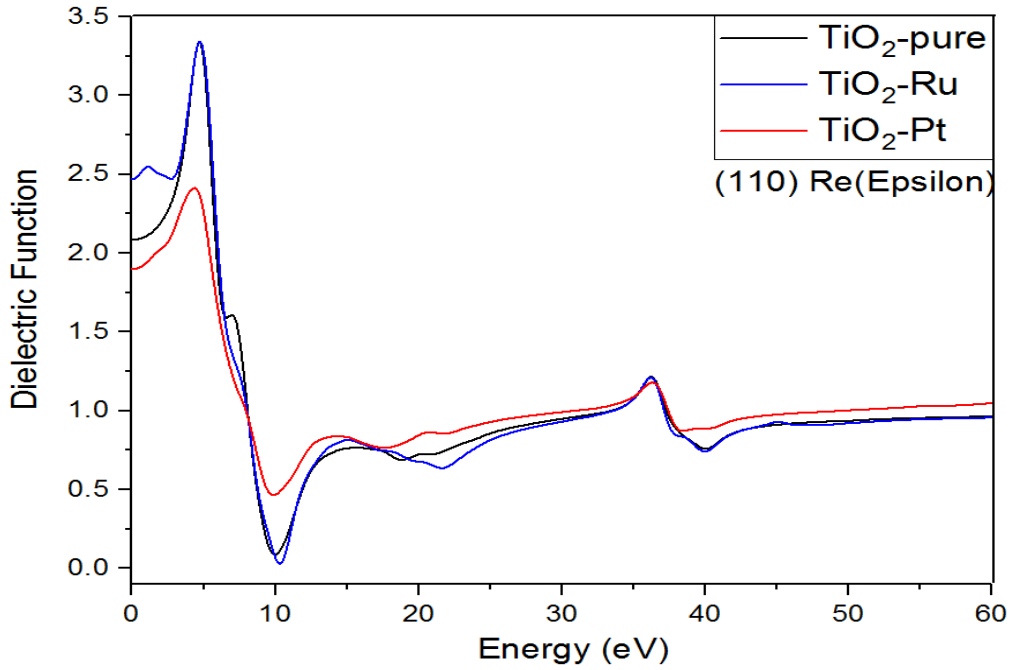

Figure 4. 32 Real part of dielectric function of the undoped and doped brookite TiO_2 (110) surface.

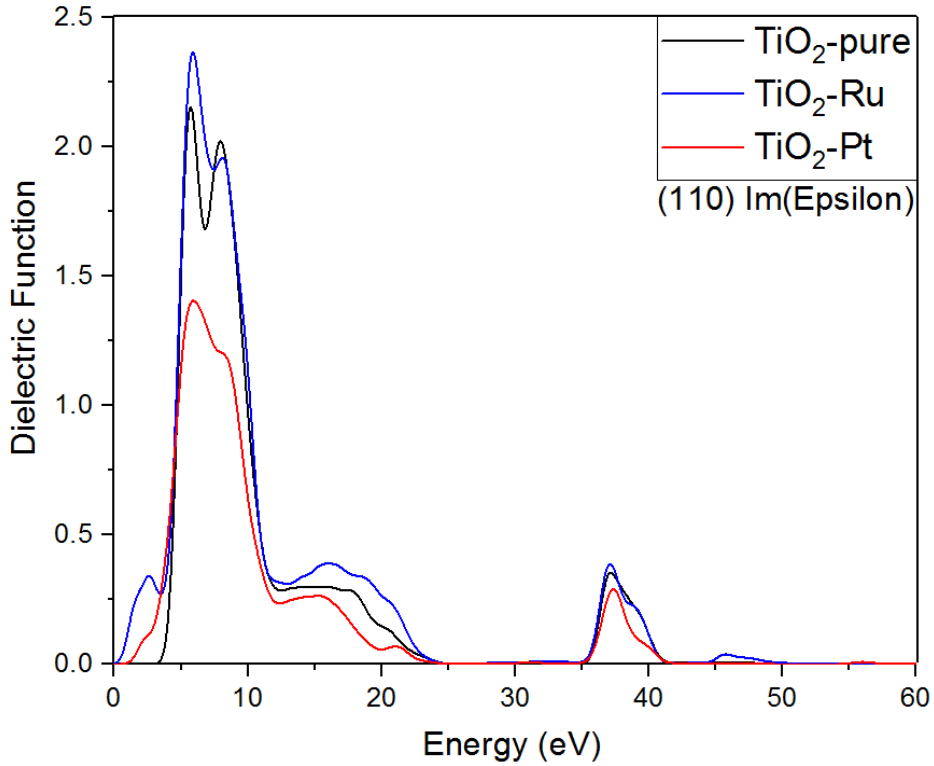

Figure 4. 33 Imaginary part of dielectric function of the undoped and doped brookite TiO_2 (110) surface.

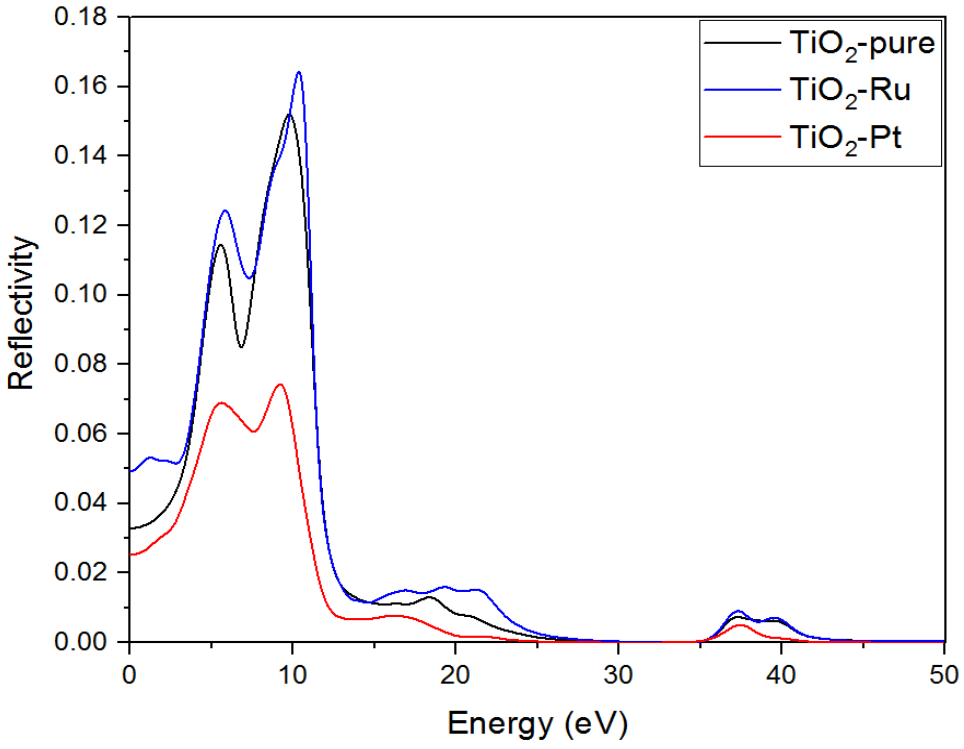

Figure 4. 34 Reflection spectrum of the undoped and doped brookite TiO_2 (110) surface.

The reflectivity spectra of undoped and doped surfaces are displayed in Figure 4.34 as a function of energy. The reflectivity is much higher in the infrared region. The un-doped and doped surfaces are showing similar reflectivity spectra patterns, where the first peak is at low energy ranging between 0 to 13 eV, with some splitting at the top. The other two peaks are at ~16 eV and ~37 eV, with decreasing intensity. The intensity of these two peaks is lower than those of (100) and (210) surfaces, reported in previous subsections. For Pt doped the reflectivity spectra is showing three peaks, where all peaks are in the same energy region as those of undoped and Ru doped, but with low intensity or low photo energy in all regions.

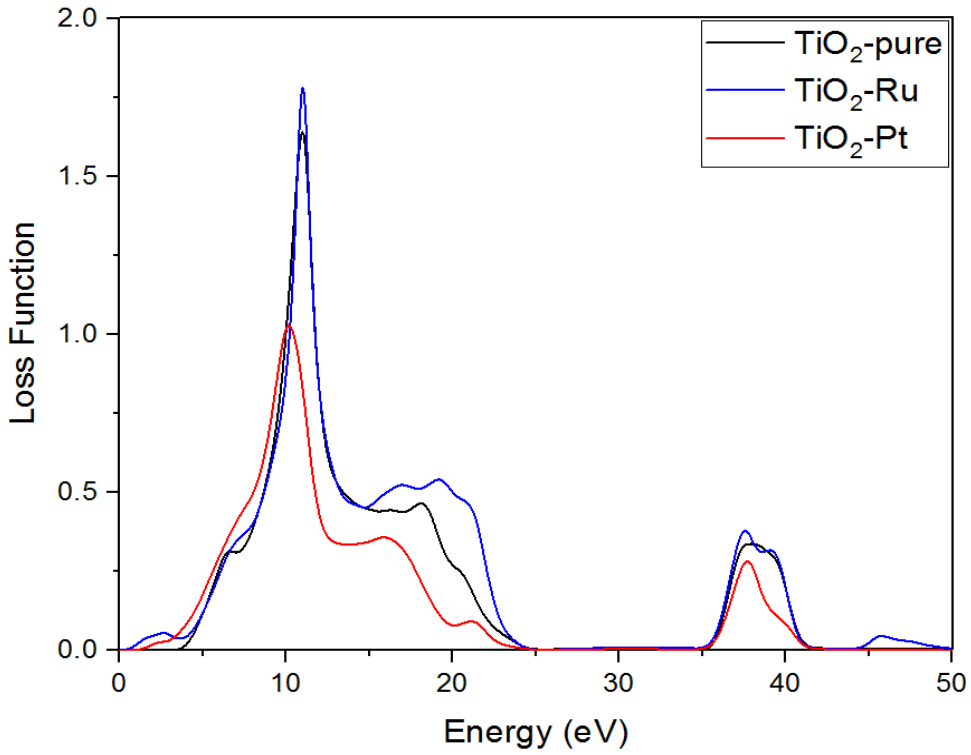

Figure 4. 35 Energy loss function of the undoped and doped brookite TiO_2 (110) surface.

The energy loss spectra of all surfaces are depicted in Figures 4.35 as a function of photon energy. For all surfaces, there are two major peaks found at 10 eV and 37 eV, which indicate the rapid reduction in the reflectance. The maximum peak is found at 10 eV for all surfaces. Hence, it is found that the plasma frequency for all surfaces is 10 eV. When the incident photon energy is higher than 40 eV, all the surfaces become transparent.

CHAPTER 5

5.1 Conclusions

First principle calculations were successfully used to investigate structural, electronic and optical properties of undoped and Ru or Pt doped brookite TiO_2 low index surfaces. Generalized gradient approximation in the scheme of Perdew-Burke-Ernzerhof (PBE) was used to describe the exchange-correlation functionals of the systems. All calculations were carried out using CASTEP code as implemented in Materials Studio of BIOVIA Inc. The kinetic energy cut-off of 650 eV and 4x4x2 k-points were determined to be the convergence parameters in this study.

The three low index surfaces of brookite TiO_2 i.e. (100), (210) and (110) surface were generated by clearing a surface from the optimized bulk structure and building a slab. The study revealed that truncation of the octahedral renders different coordination combinations for the outermost titanium cations. All the surfaces are characterized by the presence of two types of 2-fold coordinated oxygen atoms (O_{2c} and O'_{2c}) and 5-fold coordinated Ti atom (Ti_{5c}). Doping TiO_2 surfaces with Ru or Pt showed a subtle atomic rearrangement for all the surfaces.

Electronic properties for undoped and Ru or Pt doped (100), (210) and (110) surfaces were successfully investigated. Based on calculated results, the analysis of electronic structure suggests that, metal dopants shift the VBs to higher energy for all the surfaces. The results also show that owing to the formation of the impurity energy levels, which are mainly hybridized by 3d states of impurities with O 2p states or Ti 3d states, the response region in spectra could be extended to the visible light region. The components of VBs, CBs and dopant states support that the metal dopants are active in inter-band transitions induced by lower energy excitations, which is important for the application in solar energy. Transition metal doping narrowed the band gap of TiO_2, leading to improvement of the photo reactivity of TiO_2. Ru doped surface was found to have the lowest energy band gap with the values 1.143 eV, 1.335 eV and 1.331 eV for (100), (210) and (110) surfaces respectively.

The compensating optical absorbance of Ru and Pt dopants in different wavelength region presents that both dopants may possess prominent optical absorption properties. Compared with undoped TiO_2, the metal dopants shift the absorption to

longer wavelength and improve optical absorbance in visible and near-IR region, with an exception of undoped (110) which showed no activity in the visible and near IR region.

Theoretical research on transition metal-doped TiO_2 is of great importance to develop the photocatalytic applications. First-principles calculations of doped TiO_2 is still an ongoing subject, and a few challenging problems require further investigation in an urgent demand. One of the challenges is the influence of the transition metal doping on the phase transition of TiO_2 from anatase to rutile. A theoretical understanding on its mechanism will be useful to optimize the performance of TiO_2 in photocatalytic and other applications. Other methods such as virtual crystal approximation could be used to investigate doping properties, whereby small concentrations could be used, cutting down the calculation time. Computer modelling could provide more accurate theoretical models to simulate the doping mechanisms, which could lead to optimized performance of transitional metal doped TiO_2 photocatalysts.

REFERENCES

1. R. Eisenberg and D.G. Nocera, Preface: Overview of the forum on solar and renewable energy. *Inorg. Chem*. 2005, 44, 6799.
2. H. Trollip, A. Butler, J. Burton, T. Caetano and C. Godinho. Energy security in South Africa. *Cape T Maps*. 2014, 17, 1.
3. D. R. McConnell. Renewable sustainable energy. 2002, 6, 273.
4. J. Yang, Z. Fan and M. Sheng. Solar cells - dye-sensitized devices. *InTech*. 2011, 2, 307-735.
5. M. Grätzel. Solar Energy conversion by dye-sensitized photovoltaic cells, *Inorg. Chem*. 2005, 44(20), 6841.
6. http://www.businesswire.com/news/home/20170727006497/. First Solar, Inc. First solar, Inc. Announces fourth quarter and 2011 financial B results (Press Release), Retrieved February 28, 2017.
7. S. Rühle. Tabulated values of the Shockley-Queisser limit for single junction solar cells. *Solar Energy*. 2016, 13, 139.
8. W. Shockley, H. Queisser. Detailed balance limit of efficiency of p-n junction solar cells. *J. Appl. Phys.* 1961, 32, 510.
9. https://energy.gov/eere/sunshot/downloads/research-cell-efficiency-records. National renewable energy laboratory (2012), Research cell efficiency records.
10. C.J. Wang, R.L. Thompson, J. Baltrus and C. Matranga. Prospects of CO_2 utilization via direct heterogeneous electrochemical reduction. *J. Phys. Chem. Lett*. 2010, 1, 48.
11. F.E. Osterloh, B.A. Parkinson. Recent developments in solar water-splitting photocatalysis. *MRS Bull*. 2011, 36, 17.
12. K. Maeda and K. Domen. Photocatalytic water splitting: Recent progress and future challenges. *J. Phys. Chem. Lett*. 2010, 1, 2655.
13. M. Grätzel. Review article photo electrochemical cells. Nature 2001, 414, 338.
14. B. O'Regan and M. Gratzel. Low-cost, high-efficiency solar cell based on dye-sensitized colloidal TiO_2 films. *Nature* 1991, 353, 737.
15. L. Kavan, M. Grätzel. S.E. Gilbert, C. Klemenz and H. Scheel. Electrochemical and photo electrochemical investigation of single-crystal anatase. *J. Am. Chem. Soc.* 1996, 118, 6716.

16. X. Bokhimi, A. Morales, M. Aguilar, J.A. Toledo-Antonio and F. Pedraza. Local order in titania polymorphs. *Int. J. Hydrogen Energy.* 2001, 26, 1279.
17. D. Cahen, G. Hodes, M. Grätzel, J.F. Guillemoles, I. Riess. Nature of photovoltaic action in dye-sensitized solar cells. *J. Phys. Chem*. B 2000, 104, 2053.
18. A. Hagfeldt, G. Boschloo, L.C. Sun, L. Kloo and H. Pettersson. Dye-sensitized solar cells. *Chem. Rev*. 2010, 110, 6595.
19. R. Jose, V. Thavasi, S. Ramakrishna. Highly efficient dye-sensitized solar cell prepared by electrophoretic deposition method: the effect of TiO_2 films thickness on the performance of cells. *J. Am. Ceram. Soc*. 2009, 92, 289.
20. Y.Q. Zheng, E.R. Shi, Z.Z. Chen, W.J. Li and X.F. Hu. Synthesis and li-ion insertion properties of highly crystalline mesoporous Rutile TiO_2. *J. Mater. Chem.* 2001, 11, 1547.
21. M.K. Nazeeruddin, F. De Angelis, S. Fantacci, A. Selloni, G. Viscardi, P. Liska, S. Ito, T. Bessho and M. Gratzel. Combined experimental and DFT-TDDFT computational study of photoelectrochemical cell ruthenium sensitizers. *J. Am. Chem. Soc*. 2005, 127, 16835.
22. Y. Wang, F. Gao, D. Shi, J. Zhang, M.K. Wang, X.Y. Jing. Humphry-Baker, R. Wang, P. Zakeeruddin and S.M. Gratzel. Enhance the optical absorptivity of nanocrystalline TiO_2 film with high molar extinction coefficient ruthenium sensitizers for high performance dye-sensitized solar cells. *J. Am. Chem. Soc*. 2008, 130, 10720.
23. A. Fujishima and K. Honda. Intensity effects in the electrochemical photolysis of water at the TiO_2 electrode. *Nature.* 1972, 238, 37.
24. M.I. Litter. Heterogeneous photocatalysis: Transition metal ions in photocatalytic systems. *Appl. Catal. B-Environmental.* 1999, 23, 89.
25. M. Ni, M.K. Leung, D. Y. C. Leung, K. Sumathy. A review and recent developments in photocatalytic water-splitting using TiO_2 for hydrogen production. *Renewable Sustainable Energy Rev*. 2007, 11, 401.
26. O. Glemser and E. Schwarzmann. Zur polymorphie des titandioxyds. *Angew. Chem*. 1956, 68, 791.
27. X. Bokhimi, A. Morales, M. Aguilar, J.A. Toledo-Antonio and F. Pedraza. Local order in titania polymorphs. *Int. J. Hydrogen Energy.* 2001, 26, 1279.
28. S. Yamaguchi. Brookite film on titanium. *J. Electrochem. Soc*. 1961, 108, 302.

29. H. Kominami, M. Kohno, Y. Kera Synthesis of brookite-type titanium oxide nano-crystals in organic media. *J. Mater. Chem*. 2000, 10, 1151.
30. J.H. Lee and Y.S. Yang. Effect of HCl concentration and reaction time on the change in the crystalline state of TiO_2 prepared from aqueous $TiCl_4$ solution by precipitation, *J. Euro. Ceram. Soc*., 2005, 25, 3573.
31. I. Keesmann. Zur hydrothermalen synthese von brookit. *Z. Anorg. Allg. Chem*. 1966, 346, 30.
32. H. Yang, J. Li, G. Zhou, S. W. Chiang, H. Du, L. Gan, C. Xu, F. Kanga and W. Duande. First principles study of ruthenium (II) sensitizer adsorption on anatase TiO_2 (001) surface, *RSC Adv*. 2015, 5, 60230.
33. M. Grätzel and F.P. Rotzinger. The influence of the crystal lattice structure on the conduction band energy of oxides of titanium (IV). *Chem. Phys. Lett*. 1985, 118, 474.
34. R. Zallen and M.P. Moret. The optical absorption edge of Brookite TiO_2, *Sol State Comm*. 2006, 137,154.
35. S .D. Mo and W. Y. Ching. Electronic and optical properties of three phases of titanium dioxide: Rutile, anatase and brookite. *Phys. Rev. B* 1995, 51, 13023.
36. D. Dung, J. Ramsden and M. Grätzel. Dynamics of interfacial electron-transfer processes in colloidal semiconductor systems. *J. Am. Chem. Soc*. 1982, 104, 2977.
37. T.A. Kandiel, A. Feldhoff, L. Robben, R. Dillert and D.W. Bahnemann. Tailored titanium dioxide nanomaterials: Anatase nanoparticles and brookite nanorods as highly active photocatalysts. *Chem. Mater*. 2010, 22, 2050.
38. Kang, K. Kim, S. C. Yu and H. Chae. First-principles study for ferromagnetism of Cu-Doped ZnO with carrier doping, *J. Soli. State Chem*., 2013, 198, 120.
39. J. Park, C. Lee, K. Jung and D. Jung. Structure related photocatalytic properties of TiO_2. Bull. *Korean Chem. Soc*. 2009, 30, 3788.
40. D.A.H. Hanaor, M.H.N. Assadi, S. Li, A. Yu, and C.C. Sorrell. Ab initio study of phase stability in doped TiO_2. *Comp. Mech*. 2012, 2, 185.
41. W.K. Li, X.Q. Gong, G. Lu and A. Selloni. Different reactivity's of TiO_2 polymorphs: comparative DFT calculations of water and formic acid adsorption at anatase and brookite TiO_2 surfaces. *J. Phys. Chem*. C 2008, 112, 6594.
42. N. Serpone and E. Pelizzetti. Photocatalysis fundaments and application, *second ed. Wiley-Interscience, New York*, 1989, p. 236.

43. J.C. Yang, Y.C. Kim, Y.G. Shul, C.H. Shin and T.K. Lee. Characterization of photoreduced Pt/TiO_2 and decomposition of dichloroacetic acid over photoreduced Pt/TiO_2 catalysts. *Appl. Surf. Sci*. 1997, 525.
44. A.V. Vorontsov, I.V. Stoyanova, D.V., Kozlov, V.I. Simagina and E.N. Savinov. Kinetics of the photocatalytic oxidation of gaseous acetone over platinized titanium dioxide. *J. Catal. B*. 2000, 43, 360.
45. M.R. Hoffmann, S.T. Martin, W.Y. Choi and D.W. Bahnemann. Environmental applications of semiconductor photocatalysis. *Chem. Rev*. 1995, 95, 69.
46. J. Feng, Y. Jiao, W. Ma, M.D. K. Nazeeruddin, M. Grätzel and S. Meng. First principles design of dye molecules with ullazine donor for dye-sensitized solar cells, *J. Phys. Chem*. 2013, 8, 3772.
47. E. Finazzi, C. Di Valentin, A. Selloni and G. Pacchioni. First principles study of nitrogen doping at the anatase TiO_2 (101) surface, *J. Phys. Chem*. C, 2007, 26, 9275.
48. Q. Chen, C. Tang, G. Zheng. First-principles study of TiO_2 anatase (101) surfaces doped with nitrogen. *Phys B*. 2009, 404, 1074.
49. Y. Yang, Q. Feng, W. Wang, and Y. Wang. First-principle study on the electronic and optical properties of the anatase TiO_2 (101) surface, *J. Semi*. 2013, 34, 1674.
50. M. Kogo M, Y. Sanehira, M. Ikegamia and T. Miyasaka. Brookite TiO_2 as a low-temperature solution-processed mesoporous layer for hybrid perovskite solar cells, *J. Mater. Chem.* 2015, 3, 20952.
51. M. Landman, E. Rauls, W.G Schmidt. The electronic structure and optical response of rutile, anatase, and brookite TiO_2. J. Phys 2012, 24, 8953.
52. L. H. Thomas. The calculation of atomic fields, Proc. *Camb. Phil. Soc*. 1927, 23, 542.
53. E. Fermi, "Un metodo statistico per la determinazione di alcune priorieta dell'atome", *Rend. Accad. Naz*. 1927, 196, 602.
54. W. Kohn and L.J. Sham. Self-consistent equations including exchange and correlation effects. *Phys. Rev. A*. 1965, 140, 1133.
55. O. Gunnarsson and B.I. Lindqvist. Exchange and correlation in atoms, molecules, and solids by the spin-density-functional formalism. *Phys. Rev. B*. 1976, 13, 4174.

56. D.C. Langreth and J.P. Perdew. The exchange-correlation energy of a metallic surface: wavevector analysis. *Phys. Rev. B*. 1977, 15, 2884.
57. B.W. Dadson. Development of a many-body Tersoff-type potential for silicon *Phys. Rev. B*. 1987, 35, 880.
58. K.-M. Ho and K.P. Bohnen. Stability of the missing-row reconstruction on fcc (110) transition-metal surfaces. *Phys. Rev. Lett*. 1987, 59, 1122.
59. N. Martsinovich, D. R. Jones, and A. Troisi. Electronic structure of TiO_2 surfaces and effect of molecular adsorbates using different DFT implementations. *J. Phys. Chem.* 2010, 114, 22659.
60. P. Perdew and Y. Wang. Accurate and simple density functional for the electronic exchange energy: Generalized gradient approximation. *Phys. Chem. Rev*. 1986, 33, 8800.
61. B. G. Johnson, P. M. W. Gill, J. A. Pople. The performance of a family of density functional. *J. Chem. Phys*. 1993, 98, 5612.
62. T. Ziegler. Approximate density functional theory as a practical tool in molecular energetics and dynamics. *Chem. Rev. B*. 1991, 91, 651.
63. T. V. Russo, R. L. Martin, P. J. Hay. Density functional calculations on first-row transition metals. *J. Chem. Phys*. 1994, 101, 7729.
64. M. Eder, E.G. Moroni and J. Hafner. Structural, electronic and magnetic properties of thin Mn films on Cu (100) substrates. *Phys. Rev. B*. 2000, 61, 11 492.
65. J.C. Phillips. Energy-band interpolation scheme based on a pseudopotential. *Phys. Rev*. 1958, 112, 685.
66. M.L. Cohen and V. Heine, The fitting of pseudopotentials to experimental data and their subsequent application. *Solid State Phys*. 1970, 24, 37.
67. H. Hellmann. A new approximation method in the problem of many electrons, *J. Chem. Phys*. 1935, 3, 61.
68. M.C. Payne, M.P. Teter, D.C. Allan, T.A. Arias and J.D. Joannopoulos. Iterative minimization techniques for ab initio total-energy calculations: molecular dynamics and conjugate gradients. *Rev. Mod. Phys*. 1992, 64, 1045.
69. L. Kleinmann and D.M. Bylander. Efficacious form for model pseudopotentials. *Phy. Rev. B*.1982 48, 1425.
70. D. Vanderbilt. Soft self-consistent pseudopotentials in a generalized eigenvalue formalism. *Phys. Rev. B*. 1990, 41, 7892.

71. V. Milman, B. Winkler, J.A. White, C.J. Peak ard, M.C. Payne, E.V. Akhmatskaya and R.H. Nobes. Electronic structure, properties, and phase stability of inorganic crystals: A pseudopotential plane-wave study. *Int. J. Quant. Chem*. 2000, 77, 895.
72. M.D. Segall, P.L.D. Lindan, M.J. Probert, C.J. Peak ard, P.J. Hasnip, S.J. Clark and M.C. Payne. First-principles simulation: ideas, illustrations and the CASTEP code. *J. Phys. Cond. Matt*. 2002, 14, 2717.
73. J. Harris and R.O. Jones. The surface energy of a bounded electron gas. *J. Phys.* 1974, 4, 1170.
74. M. Koelsch, S. Cassaignon, J. F. Guillemoles, and J. P. Jolivet. Comparison of optical and electrochemical properties of anatase and brookite TiO_2 synthesized by the sol-gel method. *Thin Solid Films*. 2002, 312.
75. A. Beltra´n, L. Gracia, and J. Andre´s. Density functional theory study of the brookite surfaces and phase transitions between natural titania polymorphs. J. *Phys. Chem*. 2006, 110, 23417.
76. E.P. Meagher, G.A. Lager. Polyhedral thermal expansion in the TiO_2 polymorphs; refinement of the crystal structures of rutile and brookite at high temperature Can. *Mineral*. 1979, 17, 77.
77. J.S. De Almeida and R. Ahuja. Electronic and optical properties of RuO_2 and IrO_2. *Phys. Rev. B*. 2006, 73, 165102.